

# Grid-Forming Inverters: A Comparative Study of Different Control Strategies in Frequency and Time Domains

**NABIL MOHAMMED**  (Senior Member, IEEE), **HARITH UDAWATTE**  (Graduate Student Member, IEEE),  
**WEIHUA ZHOU**  (Member, IEEE), **DAVID J. HILL**  (Life Fellow, IEEE),  
**AND BEHROOZ BAHRANI**  (Senior Member, IEEE)

Department of Electrical and Computer Systems Engineering, Monash University, Clayton, VIC 3800, Australia

CORRESPONDING AUTHOR: NABIL MOHAMMED (e-mail: nabil.mohammed@ieee.org)

This work was supported in part by Australian Renewable Energy Agency under Grant 2023/ARP010 and in part by Australian Research Council under Grant DP230100801.

**ABSTRACT** Grid-forming inverters (GFMI) are anticipated to play a leading role in future power systems. In contrast to their counterpart grid-following inverters, which employ phase-locked loops for synchronization with the grid voltage and rely on stable grid connections, GFMI primarily employ the power-based synchronization concept to form the voltage. Hence, they can not only stably operate in regions of the grid characterized by low strength but also provide critical ancillary services to power systems, including voltage, frequency, and inertia support. Several control strategies have been employed for GFMI, making it crucial to comprehend their stability characteristics for the analysis of small-signal stability and low-frequency oscillations. This article examines the performance of GFMI when equipped with four different control strategies, namely, droop-based GFMI, virtual synchronous generator (VSG)-based GFMI, compensated generalized VSG (CGVSG)-based GFMI, and adaptive VSG (AVSG)-based GFMI. The comparative analysis assesses the performance and robustness of these four control strategies across various operational scenarios in frequency and time domains. Initially, the impedance-based stability analysis method is employed to evaluate these control strategies across different case studies in terms of grid strengths, grid impedance ratios, the dynamics with/without virtual impedance and inner voltage and current loops, and variations in the inverter's operating points. Subsequently, time-domain verification using the electromagnetic transient models is conducted for these case studies as well as to assess the power tracking capability of these control strategies in response to changes in power references. Finally, the robustness of these four controllers is explored against external grid disturbances, including grid frequency deviations, phase jumps, and voltage sags, considering varying levels of disturbance magnitudes in both weak and strong grid connections. In conclusion, the evaluation of these control techniques in various operational scenarios reveals their strengths and weaknesses, offering valuable guidance for the selection of the most appropriate control technique to suit desired practical applications.

**INDEX TERMS** Droop control, grid disturbance, grid-forming inverters (GFMI), small signal, stability analysis, strong grid, virtual synchronous generator (VSG), weak grid.

## NOMENCLATURE

IBR	Inverter-based resource.	SCR	Short-circuit ratio.
PCC	Point of common coupling.	GFL	Grid following.
PSC	Power synchronization control.	GFM	Grid forming.
PI	Proportional–integral.	GFMI	Grid-forming inverters.
PLL	Phase-locked loop.	GFLI	Grid-following inverters.
PWM	Pulsewidth modulation.		

VSG	Virtual synchronous generator.
CGVSG	Compensated generalized virtual synchronous generator.
AVSG	Adaptive virtual synchronous generator.
VOC	Virtual oscillator control.
RoCoF	Rate of change of frequency.
APC	Active power controller.
RPC	Reactive power controller.

## I. INTRODUCTION

The transformation of current power systems is being driven by the rise of IBRs, as renewable energy sources such as solar and wind are being utilized to replace traditional fossil-fuel-based synchronous generators, thereby contributing to emissions reduction. The pivotal role in ensuring the stability and reliability of the grid is increasingly being taken on by these IBRs [1], [2]. In this context, control technologies for IBRs are seen to play a critical role in facilitating the seamless integration of renewable energy sources, thereby significantly impacting grid stability.

Currently, the majority of IBRs are operated in the GFL mode, relying on grid synchronization techniques, such as the utilization of the PLL [3]. This mode is designed to have the grid voltage followed and current injected as necessary, resulting in a current-source-like behavior exhibited by GFLIs. This feature distinguishes GFLIs from synchronous generators, which are acted upon as voltage sources at a fixed frequency. Due to the high dependence of GFLIs on the PLL, undesirable performance in terms of low-frequency oscillation that may even lead to eventual instability is observed in the GFL mode under weak grid conditions, which are anticipated in future power networks [4]. Therefore, their capability to strengthen the grid in a future IBR-dominated power system is limited. As a result, GFMI are being developed and commercially deployed as an emerging solution to provide voltage and frequency regulation in a power system without synchronous generators. Unlike GFLIs, voltage-source behavior is emulated by GFMI, with their primary objective being the maintenance of the internal voltage phasor [5]. Consequently, GFMI are well suited for the delivery of ancillary services to the grid, akin to synchronous generators, even in weak grid scenarios.

Although the concept of GFMI originally emerged for islanded microgrids, the control of these inverters can be configured to operate in either islanded or grid-connected mode. In islanded microgrids dominated by IBRs, one or more inverters must operate as voltage sources to establish and energize the local power grid [6], [7]. However, the increasing penetration of IBRs has made it necessary for GFMI to emulate synchronous generator characteristics even in the grid-tied mode, as the system's inertia reduces and frequency stability becomes a major concern [8]. Grid-connected GFMI employ power-based synchronization mechanisms, relying on the relationship between active power and frequency through a primary control loop to interact with the grid [9].

The GFM control methodologies can be broadly classified into two types: droop-based control and synchronous-machine-based control [5]. Different variations of GFM control methods can be found in the literature and can be categorized within the aforementioned classifications. On the one hand, droop, which is based on mimicking the operation of synchronous generators, is one of the most mature control techniques. It includes three categories based on the control law: frequency-based droop [10], [11], angle-based droop [12], [13], and PSC [14], [15]. On the other hand, synchronous-machine-based control is introduced to address the primary drawback of droop methods, which is the absence of inertia support. Various concepts have been developed to mimic the behavior of synchronous generators, such as virtual synchronous machine [16], [17], VSG [18], [19], and synchronverter [20], [21].

In addition to these conventional droop and VSG methods, several other approaches have been proposed for GFMI, primarily designed using nonlinear control techniques. VOC [22], [23],  $H_\infty$ -based methods [24], [25], and virtual synchronous control utilizing dc-link capacitor dynamics [26] are examples of other popular control techniques. However, in this article, focus is placed on the most widely used methods for GFMI, which are the frequency-based droop method and VSG-based methods, as they exhibit promising features and can be considered well-established control techniques [27].

Recently, the CGVSG and the AVSG have been introduced in [28] and [29], respectively. The CGVSG and AVSG are put forth as solutions addressing the deficiencies identified in the VSG, ensuring the stable operation of GFMI in both weak and strong grid connections. The primary objective of both the CGVSG and the AVSG is the accurate tracking of power references and the achievement of desired dynamic performance. This is accomplished by taking into consideration grid parameters during the design phase. The CGVSG employs a lead-lag compensator to guarantee a predefined RoCoF limit and minimized overshoots. In contrast, the VSG structure is adopted by the AVSG; however, its parameters are adaptively tuned based on the real-time estimation of grid impedance. This adaptive approach ensures robust performance across various grid scenarios while adhering to predefined settling time and damping.

With such variations of GFM control methods proposed in the literature, it becomes essential to compare their performance and identify their limitations. While detailed comparisons among GFL control techniques have been carried out [30], [31], there is a lack of such studies for GFMI. Previous articles [32], [33] provide overviews of GFM control schemes such as droop, VSG, PSC, and VOC, outlining their limitations. However, these articles primarily focus on the structural differences among various GFM approaches rather than performance evaluation. Similar reviews are found in [34] and [35], presenting future challenges in GFM methods and emphasizing control differences among state-of-the-art techniques. Meanwhile, in [36], a comparative performance analysis between droop- and oscillator-based GFM converters

shows the superiority of oscillator-based methods in steady-state response, transient stability, and harmonic compensation. Notably, VSG-based controllers, designed to overcome droop limitations, are not considered in this study. In addition, in [37], a performance evaluation assesses four GFM control strategies with a primary focus only on their soft black-start capabilities.

Evaluation of these controllers can be conducted from both small- and large-signal viewpoints. For instance, in [38], the dynamic characteristics of droop- and VSG-based GFMI are analyzed using two developed small-signal models. This study also examines oscillation phenomena in output active power using state-space models, highlighting the advantages of VSG over droop in both grid-connected and stand-alone modes. A complementary study in [39] compares matching and dispatchable VOC methods against classical synchronous machine emulation techniques under various grid conditions. The study evaluates dominant eigenvalues. In [40], an impedance-based black box strategy is employed to determine the robustness of the controllers. However, the study is limited to droop-based controllers. Furthermore, in [41], variations in microgrid dynamics are observed between two droop methods, i.e., single-loop and multiloop, despite their similar control mechanisms. Yet, the study is limited only to droop-based controllers.

Beyond the aforementioned frequency-domain analysis, the performance evaluation of GFMI in the time domain is carried out from a large-disturbance stability perspective in [42]. Factors such as grid disturbances and faults, as well as the dynamics of current limitation, come into play in large-signal models. In [43], a design-oriented study is presented to characterize the transient behavior of PSC, droop, droop with a low-pass filter, and VSG methods. The study compares the responses of these controllers for power reference changes and voltage sag at the PCC. However, other possible grid disturbances, such as frequency and phase jumps, are not considered. In addition, the impact of virtual impedance and current limiting algorithms in GFMI is discussed in [44] for a three-phase to ground fault. Notably, this work is limited to droop-based controllers, even though virtual-impedance-related dynamics may have distinct effects on various GFM control methods.

In summary, the existing comparison studies of different control techniques of GFMI tend to focus on specific aspects, such as differences in control structure, small-signal stability, or large-signal stability. However, there is a critical need for a comprehensive evaluation of these control techniques across various grid conditions and test cases within a single study, as they exhibit different responses. Furthermore, to date, no efforts have been undertaken to compare the performance of the two state-of-the-art control techniques, namely, the CGVSG and the AVSG, both of which demonstrate promising performance in different grid connections. To address this gap, a thorough analysis is aimed to be conducted in this article, providing researchers with a deeper understanding of different control methods employed in GFMI systems.

This article presents a detailed examination of four distinct control strategies employed in GFMI: droop, VSG, CGVSG, and AVSG. The key contributions of this study are as follows:

- 1) *frequency-domain analysis*: detailed examination of four control methods for GFMI in both weak and strong grid scenarios, using Bode and Nyquist plots. Analysis includes variations in SCR, variations in grid impedance ratio, dynamics of virtual impedance, dynamics of inner current and voltage loops, and variations in the inverter operating point;
- 2) *time-domain simulations*: validation of frequency-domain results through electromagnetic transient model simulations, demonstrating practical applicability;
- 3) *analysis of grid disturbances*: evaluation of the responses of these control strategies to external grid disturbances like frequency deviations, phase shifts, and voltage sags, in both weak and strong grid connections;
- 4) *comparative assessment of control techniques*: insightful analysis of the strengths and weaknesses of each control method across different operational scenarios.

The rest of this article is organized as follows. Section II details the generic model of the GFMI, considering inner current and voltage loops, virtual impedance, and the utilization of the four control strategies within the primary loop. Section III presents a comprehensive evaluation of these strategies in the frequency domain under various conditions. Section IV covers time-domain simulation results, validates the frequency-domain analysis, and compares the performance of these control strategies. Section V presents time-domain simulation results to assess the responses of these control strategies to various external grid disturbances. Section VI summarizes the findings from the detailed examinations of the four control strategies in time and frequency domains and provides recommendations. Finally, Section VII concludes this article.

## II. MODELING OF GFMI

Fig. 1 illustrates the generic control structure of a GFMI. This inverter is supplied with a constant dc source, typically a battery. To facilitate its integration with the utility grid, the inverter incorporates an inductance-capacitive (LC) filter characterized by inductance ( $L_f$ ) with an internal resistance ( $R_f$ ), and capacitance ( $C_f$ ). The grid is represented as an ideal voltage source ( $v_g$ ) with a Thevenin equivalent impedance, composed of the grid resistance ( $R_g$ ) and grid inductance ( $L_g$ ).

The control objective of the GFMI is to regulate the injection of active power ( $P_{pcc}$ ) and reactive power ( $Q_{pcc}$ ) at the PCC into the grid to match desired references of active power ( $P_{ref}$ ) and reactive power ( $Q_{ref}$ ).

The GFMI deploys a cascaded control architecture, including several essential control loops within its operational framework. The fundamental building blocks of this architecture include the inner current control loop, the voltage loop, the virtual impedance control mechanism, and the primary loop. These interconnected control loops work synergistically to regulate its output power and form the PCC voltage. In

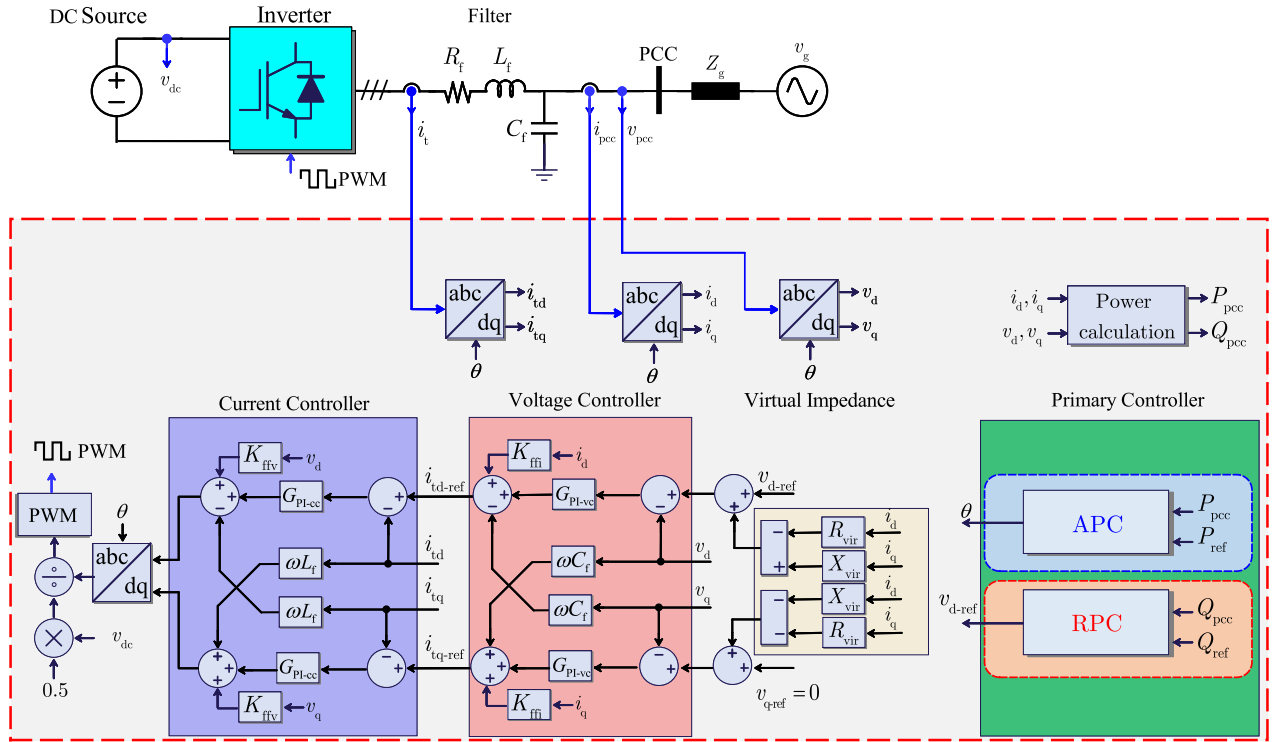


**FIGURE 1.** Generic block diagram of the GFMI under investigation.

subsequent sections, further details of each control loop are presented to provide a thorough understanding of the functionalities, control, and tuning of the GFMI.

### A. CURRENT CONTROL LOOP

The current control loop in the GFMI plays a pivotal role in ensuring reliable and efficient operation. Its core functionality is safeguarding semiconductor devices and other electrical equipment by limiting the inverter output current within permissible boundaries.

The current control loop comprises six input signals and two output signals. The  $i_{td}$  and  $i_{tq}$  signals correspond to the direct ( $d$ ) and quadrature ( $q$ ) components of the measured inverter terminal current, respectively, with potential PCC usage. The  $i_{td-ref}$  and  $i_{tq-ref}$  signals are automatically generated from the outer voltage control loop. The  $v_d$  and  $v_q$  signals are, respectively, the  $d$  and  $q$  components of the measured PCC voltage, serving as voltage feedforward to enhance the inverter's dynamic performance. In addition, the current control loop incorporates decoupling terms to reduce coupling between the  $d$  and  $q$  current components. The current control loop yields two output signals,  $v_{d-pwm}$  and  $v_{q-pwm}$ , representing the  $d$  and  $q$  components of the inverter voltage references. These references are then supplied to the PWM after being divided by  $0.5v_{dc}$ .

Three control parameters are employed by the current control loop: the voltage feedforward coefficient ( $K_{ffv}$ ), the proportional term  $K_{p-cc}$ , and the integral term  $K_{i-cc}$  of the two identical PI controllers, where the  $d$  and  $q$  components

are independently regulated each by a one PI controller. The value of  $K_{ffv}$  falls within the range of  $[0, 1]$ , and typically, it is selected as 1. Both  $K_{p-cc}$  and  $K_{i-cc}$ , responsible for handling the errors between the measured and reference currents, are typically tuned based on the inverter output filter. Each PI controller is typically tuned to have a transfer function ( $G_{PI-cc}$ ) with a zero that cancels the pole of the  $R_f L_f$  circuit of the inverter output filter, as described in the following equation:

$$G_{PI-cc} = k_p \frac{L_f s + R_f}{s} = \underbrace{k_p L_f}_{K_{p-cc}} + \underbrace{k_p R_f}_{K_{i-cc}} \frac{1}{s} \quad (1)$$

where  $k_p$  is the only parameter that needs tuning. To do so, the value of  $k_p$  is gradually increased from a very small value, and the rise time of the controller is monitored upon a step change in the current until the desired rise time is achieved, considering that the vector current controller is typically capable of achieving rise times as low as 1–2 ms. In this article, a specific value of 1500 is assigned to the  $k_p$  parameter. It is worth emphasizing that proper tuning of the current control loop is considered essential to ensure a reliable and stable operation of the inverter under various operating conditions.

### B. VOLTAGE CONTROL LOOP

The voltage control loop in the GFMI has the core functionality of safeguarding semiconductor devices and other electrical equipment by limiting the inverter output voltage within permissible boundaries.



The voltage control loop comprises six input signals and two output signals. The  $v_d$  and  $v_q$  signals correspond to the  $d$  and  $q$  components of the measured PCC voltage, respectively. The voltage reference signals for the voltage control loop are  $v_{d-ref}$  and  $v_{q-ref}$ . In the absence of  $Z_{vir}$ ,  $v_{d-ref}$  is automatically generated from the primary RPC and  $v_{q-ref}$  is set to the value of 0. In the presence of  $Z_{vir}$ , a small value is being added to  $v_{d-ref}$  and  $v_{q-ref}$  to enhance the inverter stability, as will be explained in next section. The  $i_d$  and  $i_q$  signals are, respectively, the  $d$  and  $q$  components of the measured PCC current, serving as current feedforward to enhance the inverter's dynamic performance. In addition, the voltage control loop incorporates decoupling terms to reduce coupling between the  $d$  and  $q$  voltage components. The voltage control loop yields two output signals:  $i_{td-ref}$  and  $i_{tq-ref}$ .

The voltage control loop utilizes three control parameters: the current feedforward coefficient ( $K_{ff}$ ), the proportional term ( $K_{p-vc}$ ), and the integral term ( $K_{i-vc}$ ) of the two identical PI controllers. The  $d$  and  $q$  components are independently regulated by a separate PI controller. The value of  $K_{ff}$ , typically set at 0.9, falls within the range of [0, 1]. In the  $d$  and  $q$  channels, the management of errors between the measured and reference PCC voltages is the responsibility of the two identical PI controllers. Tuning of the transfer function ( $G_{PI-vc}$ ) of each PI controller in the voltage loop is generally performed to ensure a closed-loop response that is at least ten times slower than the inner current loop, thereby preventing control interaction between the voltage and current loops

$$G_{PI-vc} = K_{p-vc} + K_{i-vc} \frac{1}{s}. \quad (2)$$

It is worth emphasizing that proper tuning of the voltage control loop, including its feedforward coefficient [45], is also deemed important for the reliability of the GFMI under various operating conditions.

### C. VIRTUAL IMPEDANCE LOOP

The virtual impedance loop concept relies upon the reshaping of the inverter output impedance characteristics through the establishment of an additional feedback control loop [46]. This reshaping is achieved by adjusting the voltage reference signals  $v_{d-ref}$  and  $v_{q-ref}$  that are provided to the inner voltage loop. In the literature, the virtual impedance has been proposed for several purposes in either stand-alone or grid-connected mode. It has been widely employed to enhance stability by improving power sharing in the presence of unequal feeder impedance in a microgrid, damping oscillations, limiting current during faults, and minimizing the decoupling between active and reactive power flow, especially in resistive grids [47], [48], [49].

The virtual impedance loop takes the  $d$  and  $q$  components of the measured PCC current ( $i_d$  and  $i_q$ ) as input signals. The output of this loop is added in real time to the voltage reference signals  $v_{d-ref}$  and  $v_{q-ref}$  to achieve the desired control objective. Existing research proposes various implementations of this control approach, including virtual resistance

( $R_{vir}$ ) [50], virtual inductance ( $L_{vir}$ ) [46], and virtual complex impedance ( $Z_{vir} = R_{vir} + jX_{vir}$ ) [51]. The most widely used approach is the virtual complex impedance, also referred to as virtual impedance in the rest of this article.

A pivotal aspect to consider is the tuning of the virtual impedance. On the one hand, the allocation of a large value to the virtual impedance enhances system stability but comes at the cost of voltage quality degradation. Several approaches to tune the virtual impedance have been provided by existing research, including setting fixed values and using adaptive approaches [52], [53], [54]. The goal is to address the tradeoff between improving inverter performance and voltage degradation. Additional insights into virtual impedance tuning are available in [49]. In this article, the virtual impedance, as depicted in Fig. 1, is utilized to enhance the performance of the GFMI operating in the grid-connected mode. This results in the suppression of oscillations, particularly in strong grid scenarios, and the stabilization of the inverter within resistive grids.

### D. PRIMARY CONTROL

The primary control objective of the GFMI is to regulate the injection of  $P_{pcc}$  and  $Q_{pcc}$  at the PCC into the grid to match the desired references  $P_{ref}$  and  $Q_{ref}$ . This control objective is typically achieved via two controllers: APC and RPC. Initially, it employs measurements of voltage and currents ( $v_{pcc}$ ,  $i_{pcc}$ ) to compute  $P_{pcc}$  and  $Q_{pcc}$ . Then, the APC regulates the real power output of the inverter to match the reference value,  $P_{ref}$ , by adjusting the phase angle ( $\theta$ ) of  $v_{pcc}$ , while the RPC regulates the flow of reactive power by adjusting the magnitude  $V_{d-ref}$  of  $v_{pcc}$ .

GFMI are categorized into various types based on the configuration of their primary control loops. These types include droop, VSG, and VOC, and other variations. In this article, the focus is directed toward an in-depth exploration of four specific control strategies: droop, VSG, CGVSG, and AVSG. The subsequent subsections provide comprehensive insights into these four control strategies, explaining the control parameters associated with each.

#### 1) DROOP-BASED GFMI

Fig. 2(a) illustrates the block diagram of the primary loop of a GFMI equipped with the conventional primary droop. Within the APC, the active power–frequency ( $P-\omega$ ) droop coefficient (without a low-pass filter) is employed. In the RPC, the reactive power–voltage ( $Q-V$ ) droop coefficient is utilized.

The concept of the droop is one of the earliest techniques introduced to enable power inverters to operate autonomously in the islanded mode, as outlined in [55]. The objective of the droop is to emulate the operational characteristics of synchronous generators by implementing the droop strategy. This strategy automatically adjusts the frequency and voltage amplitude reference values provided to the inner current and voltage control loops.

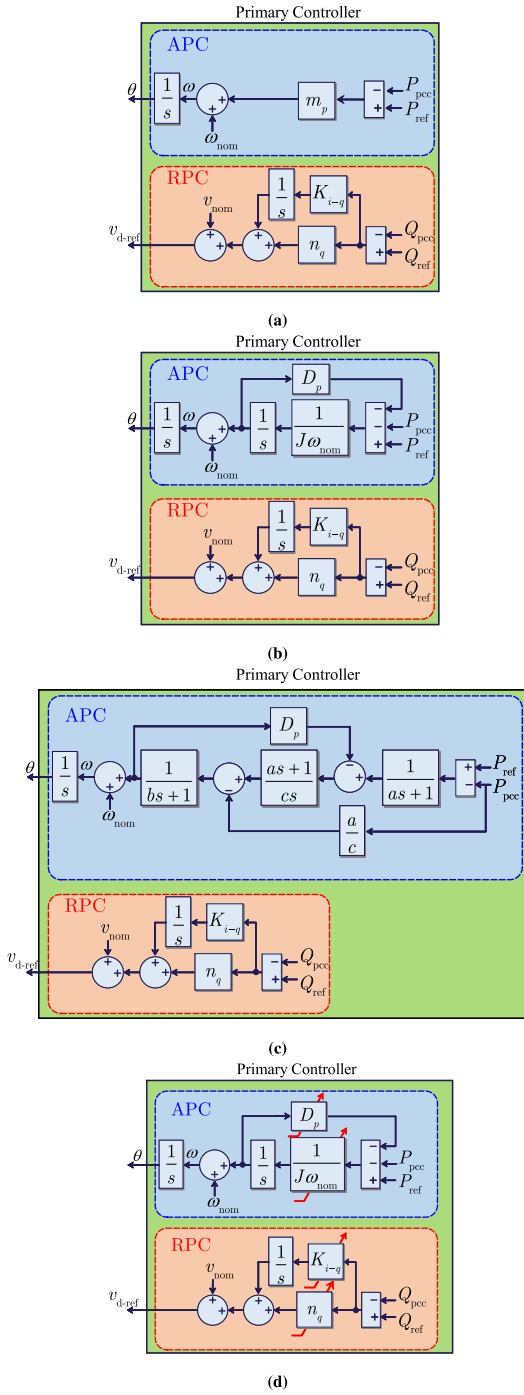


**FIGURE 2.** Control block diagrams depicting the primary loop of the GFMI considering the different control strategies under investigation. (a) Droop-based GFMI. (b) VSG-based GFMI. (c) CGVSG-based GFMI. (d) AVSG-based GFMI.

The governing equations for the active power–frequency droop and reactive power–voltage droop are given by [47]

$$\omega = \omega_{\text{nom}} + m_p(P_{\text{ref}} - P_{\text{pcc}}), \quad \theta = \int \omega dt \quad (3)$$

$$v_{\text{d-ref}} = v_{\text{nom}} + \left( n_q + \int K_{i-q} dt \right) (Q_{\text{ref}} - Q_{\text{pcc}}) \quad (4)$$

where  $\omega$  and  $v_{\text{d-ref}}$  represent the angular frequency and amplitude of the generated output voltage reference, respectively, with  $\omega_{\text{nom}}$  denotes the nominal angular frequency, while  $v_{\text{nom}}$  denotes the nominal voltage amplitude (peak-to-neutral).  $P_{\text{pcc}}$  and  $Q_{\text{pcc}}$  denote the measured output active and reactive power at the PCC, respectively, while  $P_{\text{ref}}$  and  $Q_{\text{ref}}$  are their respective reference values. The coefficients  $m_p$  and  $n_q$  for the APC and RPC are determined as follows [47], [49]:

$$m_p = \frac{\Delta\omega}{P_{\text{max}}} = \frac{2\pi(f_{\text{max}} - f_{\text{min}})}{2 \times P_{\text{rated}}} \quad (5)$$

$$n_q = \frac{\Delta V}{Q_{\text{max}}} = \frac{V_{\text{max}} - V_{\text{min}}}{2 \times Q_{\text{rated}}} \quad (6)$$

In (5) and (6),  $P_{\text{max}}$  and  $Q_{\text{max}}$  are, respectively, the maximum active and reactive power that the GFMI can either supply to the grid or absorb from the grid. As such, the factor of 2 in (4) accounts for the bidirectional power flow capability of the GFMI;  $P_{\text{rated}}$  and  $Q_{\text{rated}}$  are the rated active and reactive power of the GFMI, respectively; and  $\Delta\omega$  and  $\Delta V$  represent the maximum allowable frequency and voltage deviations, with  $f_{\text{max}}$ ,  $f_{\text{min}}$ ,  $V_{\text{max}}$ , and  $V_{\text{min}}$  specifying the associated maximum and minimum allowable frequency and voltage deviation values in accordance with grid standards.

Moreover, in situations where no automatic voltage regulator control loop is present, an integral term  $K_{i-q}$  is incorporated into the RPC during grid-connected operation, as shown in (4). This integral term ensures that the reactive power accurately tracks the desired reference with zero steady-state error.

## 2) VSG-BASED GFMI

Fig. 2(b) illustrates the block diagram of the primary loop of a GFMI equipped with the primary VSG. In contrast to the conventional droop, the VSG presents a more attractive solution due to its capacity to provide grid inertia during disturbances. Within the VSG framework, the control parameters within the APC are tuned to meet grid code specifications, including parameters such as the RoCoF, while considering operational constraints like the rated output power of the GFMI.

In the APC of the VSG control system, two control parameters are identified: damping coefficient ( $D_p$ ) and inertia coefficient ( $J$ ). The damping coefficient is calculated as the inverse of the parameter  $m_p$ , as follows:

$$D_p = \frac{1}{m_p} = \frac{2 \times P_{\text{rated}}}{2\pi(f_{\text{max}} - f_{\text{min}})}. \quad (7)$$

If the parameter  $T_{\text{VSG}}$  is linked to the desired initial RoCoF, such as within the range of 0.5–1 Hz/s, as detailed in [56] and [57], and  $\omega_{\text{nom}}$  denotes the nominal grid angular frequency, the calculation of the inertia coefficient  $J$  is carried out, as illustrated in the following equation:

$$J = T_{\text{VSG}} \times \frac{D_p}{\omega_{\text{nom}}}. \quad (8)$$

As illustrated in Fig. 2(b), the RPC employed in this article for the VSG is identical to the one utilized for the droop, as described in (4) and (6).

### 3) CGVSG-BASED GFMI

Fig. 2(c) illustrates the block diagram of the primary loop of a GFMI equipped with the primary CGVSG. This control strategy is introduced in [28] to enhance the performance of the conventional VSG, particularly in strong grids where it exhibits poor dynamic characteristics such as high overshoot and long settling time and oscillations.

In the APC of the CGVSG, the control parameters ( $a$ ,  $b$ , and  $c$ ) are calculated based on the frequency response of the open-loop system by assumes that the grid is purely inductive with a known inductance. The calculation of these control parameters is as follows:

$$a = \alpha \quad (9)$$

$$b = \frac{\beta\gamma}{\beta + \gamma - \alpha} \quad (10)$$

$$c = \frac{\beta + \gamma - \alpha}{m_p}. \quad (11)$$

For more explanation on the calculation of the parameters  $\alpha$ ,  $\beta$ , and  $\gamma$ , refer to [28]. Finally, it is worth noting that the RPC of the CGVSG used in this article is also identical to that used in the droop and the VSG, as calculated in (4) and (6).

### 4) AVSG-BASED GFMI

Fig. 2(d) illustrates the block diagram of the primary loop of a GFMI equipped with the primary AVSG. This control strategy, as proposed in [29], aims to enhance the performance of the VSG, particularly in strong grids characterized by poor dynamic performance, including high overshoot and long settling time oscillations.

Unlike the CGVSG, which assumes a purely inductive grid with a known inductance, the AVSG considers a grid model that incorporates both resistive and inductive components ( $RL$  model). It estimates the grid impedance in real time. Consequently, this approach enables the IBR to operate effectively under various grid conditions, including strong and weak grids and both inductive and resistive grids to ensure the fulfillment of predefined dynamic performance requirements.

The AVSG incorporates an event-based online active grid impedance estimation technique to accurately estimate  $R_g$  and  $L_g$ , thus minimizing power quality disturbances. The proposed control algorithm for the AVSG leverages the estimated  $R_g$  and  $L_g$  to adaptively tune both the APC and RPC, which share the same control structure as the conventional VSG. Consequently, it enhances the decoupling and control of active and reactive powers while satisfying the predefined dynamic performance criteria, including damping coefficient ( $\zeta$ ), settling time ( $T_s$ ), and, consequently, natural frequency ( $\omega_n$ ) and minimal overshoot. The control parameters of the AVSG, denoted as  $D_p$ ,  $J$ ,  $n_q$ , and  $K_{i-q}$ , are computed as follows:

$$D_p = \frac{2\zeta(1 - \sigma)K_{11}}{\omega_n} \quad (12)$$

$$J = \frac{(2 - \sigma)K_{11}}{2\omega_{nom}\omega_n^2} \quad (13)$$

$$n_q = \frac{1}{K_{22}} \quad (14)$$

$$K_{i-q} = \frac{4\zeta\omega_n}{K_{22}}. \quad (15)$$

For more detailed explanation on the adaptive tuning procedure of the AVSG parameters, refer to [29].

The subsequent detailed comparison of these four GFM technologies in frequency and time domains is presented in Sections III and IV, respectively. To ensure a fair and consistent comparison among the considered GFM technologies in each case study, the control configurations and control parameters across all systems are kept identical, with the sole variation being the primary loop. Specifically, parameters including the inner current controller, outer voltage controller, virtual impedance, and reference active and reactive power have been kept consistent/identical throughout each comparison case study under the same working conditions.

## III. FREQUENCY-DOMAIN ANALYSIS

### A. BACKGROUND ON IMPEDANCE-BASED STABILITY ANALYSIS

Frequency-domain analysis is a well-established technique for assessing the small-signal stability of power electronics converters, offering valuable insights into their dynamic behavior and performance. Such analysis is conducted using both Nyquist and Bode diagrams, which are employed to provide unique perspectives on stability assessment. Stability judgment and robustness within the complex plane are focused on by Nyquist diagrams, while detailed frequency-dependent characteristics and stability margins are provided by Bode diagrams. This process contributes to predicting system stability and improving performance through the redesign and/or retuning of control parameters. Ultimately, frequency-domain analysis facilitates the reliable integration of different IBRs within the same power grid.

In this article, the analysis of small-signal stability in the frequency domain for the four control strategies of GFMI is conducted through the utilization of the impedance-based technique. In contrast to its state-space-based counterpart, the impedance-based approach is demonstrated to offer distinct advantages. Notably, it is characterized by a reduced reliance on the need for comprehensive design information pertaining to individual inverters. Furthermore, any identification technique, such as the frequency scanning method, can be employed to acquire the impedance models for black box systems at specific points of interest, facilitating stability evaluation. This approach also allows for the incorporation of interactions between inverters and grid impedance in the analysis, thereby enhancing its depth and scope [58], [59].

The basis behind impedance-based analysis is to divide the system under study into two subsystems: source and load. Given that the GFMI can be approximated as a voltage source  $V_s(s)$  with low series output impedance  $Z_o(s)$  [5], it can be modeled by its Thevenin equivalent circuit. Similarly, the grid

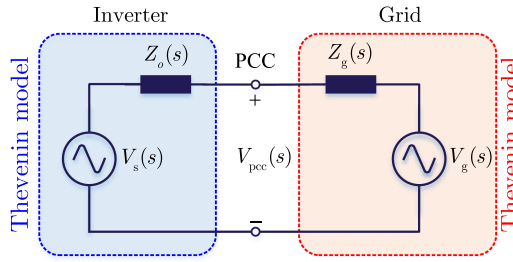


**FIGURE 3.** Small-signal impedance representation of a grid-connected GFMI system.

is also represented by the Thevenin equivalent system voltage  $V_g(s)$  and grid impedance  $Z_g(s)$ . Hence, the small-signal circuit model of the GFMI connected to the grid can be represented, as depicted in Fig. 3.

From circuit theory, the output voltage at the PCC is expressed as follows:

$$V_{pcc}(s) = \left[ V_s(s) + \frac{Z_o(s)}{Z_g(s)} V_g(s) \right] \cdot \frac{1}{1 + Z_o(s)/Z_g(s)}. \quad (16)$$

The impedance-based stability analysis can be conducted based on (16).  $V_{pcc}(s)$  is composed of two terms. It is evident that for  $V_{pcc}(s)$  to remain stable, both terms must be stable. For the first term, since the pole counts of  $V_s(s)$  and  $Z_o(s)$  are identical, the stability of the first term depends on the absence of right-half-plane poles in  $V_{pcc}(s)$ , implying that the GFMI itself is stable. The second term, which represents the interaction between the GFMI and the grid, can be conceptualized as an equivalent closed-loop system, wherein the forward gain is unity and the feedback gain is  $Z_o(s)/Z_g(s)$  [58]. Thus, the stability of the system depends on the right-hand side of

$$H(s) = \frac{1}{1 + Z_o(s)/Z_g(s)}. \quad (17)$$

In accordance with linear control theory,  $H(s)$  is stable if and only if  $Z_o(s)/Z_g(s)$  meets the Nyquist stability criterion [58]. Hence, at the intersection angular frequency ( $\omega_{int}$ ), the stability is ensured when  $\angle Z_o(j\omega_{int}) - \angle Z_g(j\omega_{int}) < 180^\circ$ . It is widely acknowledged that control strategies for power electronic converters are often developed within the  $dq$  reference frame, a choice motivated by its capacity to simplify both control design and analysis, along with its inherent advantages in understanding the dynamic behavior of the overall system. For these reasons, impedance-based studies are conducted utilizing the  $dq$  reference frame [60], [61]. Subsequently, the matrices of source impedance  $Z_o(s)$  and load impedance  $Z_g(s)$  in the  $dq$  frame can be represented as follows [30]:

$$Z_{o-dq}(s) = \begin{bmatrix} Z_{dd}(s) & Z_{dq}(s) \\ Z_{qd}(s) & Z_{qq}(s) \end{bmatrix} \quad (18)$$

$$Z_{g-dq}(s) = \begin{bmatrix} Z_{gdd}(s) & Z_{g dq}(s) \\ Z_{g qd}(s) & Z_{g qq}(s) \end{bmatrix}. \quad (19)$$

The diagonal elements in (18) and (19) are used for the stability analysis in this study due to their dominant behavior

[62]. The minor loop gains of these diagonal elements in the  $d$ -axis ( $T_{ml-dd}$ ) and in the  $q$ -axis ( $T_{ml-qq}$ ) are

$$T_{ml-dd} = Z_{dd}(s)/Z_{gdd}(s) \quad (20)$$

$$T_{ml-qq} = Z_{qq}(s)/Z_{gqq}(s). \quad (21)$$

Acquiring these necessary impedances for the stability analysis can be achieved through either analytical modeling or system identification approaches. The latter, utilized in this study, offers the advantage of accommodating commercial GFMI models and accounting for real-world operational condition changes in grid impedances [63].

The generalized Nyquist criterion, which employs a graphical representation of the system in the complex plane, is commonly utilized in control systems engineering for the assessment of feedback control system stability [58]. In the impedance-based analysis of power converters, the impedance ratios calculated from (20) and (21) are depicted using Nyquist plots to ascertain system stability [62], [64]. In summary, according to the Nyquist criterion, system stability is determined by whether the impedance ratio encircles the critical point  $(-1, 0)$ ; stability is indicated by a nonencircling behavior, while instability is indicated by encirclement. The distance from the Nyquist plot to the critical point can be utilized to derive system stability margins. Furthermore, Bode plots are employed to visualize the system analysis and to compute stability margins at the intersection point  $\omega_{int}$  of magnitudes of these impedances [65]. As explained earlier, for a stable inverter system, the phase differences of these impedances should be less than  $180^\circ$ , while the system becomes unstable when the phase differences equal or exceed  $180^\circ$ . Additional insights into the utilization of Nyquist and Bode plots for small-signal impedance-based stability analysis of grid-connected inverters are elaborated in [65] and [66].

## B. RESULTS OF IMPEDANCE-BASED STABILITY ANALYSIS

In this section, the comprehensive study in the frequency domain is presented to assess the performance of the four investigated control techniques of GFMI. The analysis of the investigated control techniques under specific conditions utilizes both Bode and Nyquist plots and is carried out in the  $dq$  reference frame, employing the GFMI's output impedance  $Z_{o-dq}$  and grid impedance  $Z_{g-dq}$ . The results are presented in five distinct sets, covering the impacts of variations in the grid SCR, the impacts of variations in the grid impedance ratio  $X_g/R_g$ , the impacts of virtual impedance ( $Z_{vir} = R_{vir} + j\omega L_{vir}$ ) and the inner voltage and current loops of GFMI, the impacts of variations in the inverter's active power reference  $P_{ref}$ , and the impacts of variations in the inverter's reactive power reference  $Q_{ref}$ . Table 1 lists the parameters of utility grid and the four GFMI under investigation. Table 2 summarizes the 11 case studies used to evaluate the performance of these GFMI in the frequency domain across the five distinct result sets.



**TABLE 1. Parameters Used for the Simulation Study**

Quantity	Value	Unit	Description
Grid parameters			
$v_g$	690	V	Grid voltage (L-L,RMS)
$f_g$	50	Hz	Nominal frequency
SCR	1.5	-	Very weak grid
SCR	2.5	-	Weak grid
SCR	8	-	Strong grid
Inverter parameters			
$S_{rated}$	5.0	MVA	Inverter rated power
$P_{rated}$	4.0	MW	Inverter rated active power
$Q_{rated}$	3.0	MVar	Inverter rated reactive power
$v_{dc}$	2000	V	DC Bus voltage
$L_f$	95	$\mu$ H	Filter inductance
$R_f$	10	m $\Omega$	Filter resistance
$C_f$	1	mF	Filter capacitance
Control parameters for the inner loops			
$K_{p-cc}$	0.1425	$\Omega$	Proportional gain of the current controller
$K_{i-cc}$	15	$\Omega/s$	Integral gain of the current controller
$K_{ffv}$	1	-	Voltage feed-forward
$k_{p-vc}$	14.25	S	Proportional gain of the voltage controller
$K_{i-vc}$	1500	S/s	Integral gain of the voltage controller
$K_{ffi}$	0.9	-	Current feed-forward
$R_{vir}$	5	m $\Omega$	Resistance of virtual impedance
$L_{vir}$	50	$\mu$ H	Inductance of virtual impedance
Droop control			
$m_p$	$0.7855 \times 10^{-6}$	rad/W.s	$P - \omega$ Droop coefficient of the APC
$n_q$	$1.5 \times 10^{-5}$	V/Var	$Q - V$ Droop coefficient of the RPC
$K_{i-q}$	$1 \times 10^{-4}$	V/Var.s	Integral gain of the RPC
VSG control			
$D_p$	$1.273 \times 10^6$	W.s/rad	Damping coefficient of the APC
$J$	4052	W.s <sup>2</sup> /rad	Inertia coefficient of the APC
$n_q$	$1.5 \times 10^{-5}$	V/Var	$Q - V$ Droop coefficient of the RPC
$K_{i-q}$	$1 \times 10^{-4}$	V/Var.s	Integral gain of the RPC
CGVSG control			
$\tau_i$	0.5	s	Inertial time constant
$n_q$	$1.5 \times 10^{-5}$	V/Var	$Q - V$ Droop coefficient of the RPC
$K_{i-q}$	$1 \times 10^{-4}$	V/Var.s	Integral gain of the RPC
AVSG control			
$\zeta$	$1/\sqrt{2}$	-	Damping coefficient
$T_s$	3	s	Settling time
$\omega_n$	0.942	rad/s	Natural frequency

**TABLE 2. Case Studies Used for the Frequency-Domain Analysis**

Case study No.	$P_{ref}$ (p.u.)	$Q_{ref}$ (p.u.)	SCR	$X_g/R_g$	Note
CS1	1	0	1.5	7	-
CS2	1	0	2.5	7	-
CS3	1	0	8	7	-
CS4	1	0	8	3	-
CS5	1	0	8	1	-
CS6	1	0	8	7	-
CS7	1	0	8	7	without $Z_{vir}$ and with inner loops without $Z_{vir}$ and without inner loops
CS8	-1	0	8	7	-
CS9	0	0	8	7	-
CS10	0	-1	8	7	-
CS11	0	1	8	7	-

## 1) IMPACTS OF GRID SCR

The impact of variations in the grid SCR on the stability and performance of GFMI is comprehensively analyzed in Fig. 4. To perform this analysis, three case studies are investigated: CS1, CS2, and CS3, corresponding to inverter connections to different grids with SCR values of 1.5, 2.5, and 8, respectively, [67]. All the cases maintain the same  $X_g/R_g$  ratio of 7, and the GFMI operates at unity power factor with reference values of  $P_{ref} = 1$  p.u. and  $Q_{ref} = 0$  p.u.

In the context of droop-based GFMI [see Fig. 4(a) and (b)], the results reveal that as the grid SCR increases, the magnitude of  $Z_{dd}$  decreases, while the magnitude of  $Z_{qq}$  increases in

the low-frequency range. Simultaneously, the phase angles of both  $Z_{dd}$  and  $Z_{qq}$  slightly decrease. This signifies that a higher grid SCR results in reduced stability margins, especially in strong grid connections. This finding is further supported by the Nyquist plots, as seen in Fig. 4(b), where the root loci of impedance ratios  $Z_{dd}/Z_{gdd}$  and  $Z_{qq}/Z_{gqq}$  approach the critical point  $(-1, 0)$  much more closely in the strong grid scenarios (CS3), represented by the red color, in contrast to weak and very weak grid scenarios, depicted by the blue and green colors, respectively.

A similar pattern is observed in the case of VSG-based GFMI, as revealed by the Bode and Nyquist plots presented in Fig. 4(c) and (d), respectively. It is noteworthy that the magnitude of the impedance of the VSG exhibits greater sensitivity to variations in the grid SCR, as depicted in Fig. 4(c). Furthermore, it is evident that the phase angle of  $Z_{qq}$  remains positive in the low-frequency range, specifically below 50 Hz, contrasting with the negative phase angle observed in droop-based GFMI. The Nyquist plots, as illustrated in Fig. 4(d), indicate a closer approach of the root loci of the impedance ratio  $Z_{qq}/Z_{gqq}$  to the critical point  $(-1, 0)$  as the grid SCR increased, predicting a deterioration in the dynamic performance of the VSG-based GFMI.

In the case of CGVSG-based GFMI depicted in Fig. 4(e) and (f), the results closely resemble those of VSG-based GFMI. Notably, the phase margin of  $Z_{qq}$  in the strong grid (indicated by red color) remains positive and consistently below  $180^\circ$  at frequencies below 50 Hz, indicating stable operation in the strong grid.

Finally, the frequency-domain results of the AVSG-based GFMI are presented in Fig. 4(g) and (h). Remarkably,  $Z_{dd}$  and  $Z_{qq}$  magnitudes vary significantly with SCR variations compared to other GFMI. Moreover, the phase angles of  $Z_{dd}$  and  $Z_{qq}$  remain positive and stay much below  $180^\circ$  at frequencies below 50 Hz, suggesting highly stable operation in strong grid connections, even surpassing CGVSG inverters. Fig. 4(h) illustrates that the root loci of the AVSG-based GFMI display minimal variations with changes in grid strength, maintaining a notable distance from the critical point  $(-1, 0)$  on the unit circle, providing additional confirmation of the AVSG-based GFMI enhanced stability.

The frequency-domain findings presented in this study of these four control strategies are further supported via time-domain simulation results, as reported next in Figs. 9 and 11. These results apply to both weak grid and strong grid operations. Reduced stability is observed in the strong grid scenario for GFMI when  $SCR = 8$  in Fig. 11, compared to the weak grid scenario with  $SCR = 1.5$  in Fig. 9.

## 2) IMPACTS OF GRID $X_g/R_g$

The impact of variations in the grid  $X_g/R_g$  ratio on the stability and performance of GFMI is comprehensively analyzed in Fig. 5. Three case studies are investigated: CS3, CS4, and CS5, corresponding to inverter connections with  $X_g/R_g$  values of 7, 3, and 1, respectively, while maintaining a constant SCR

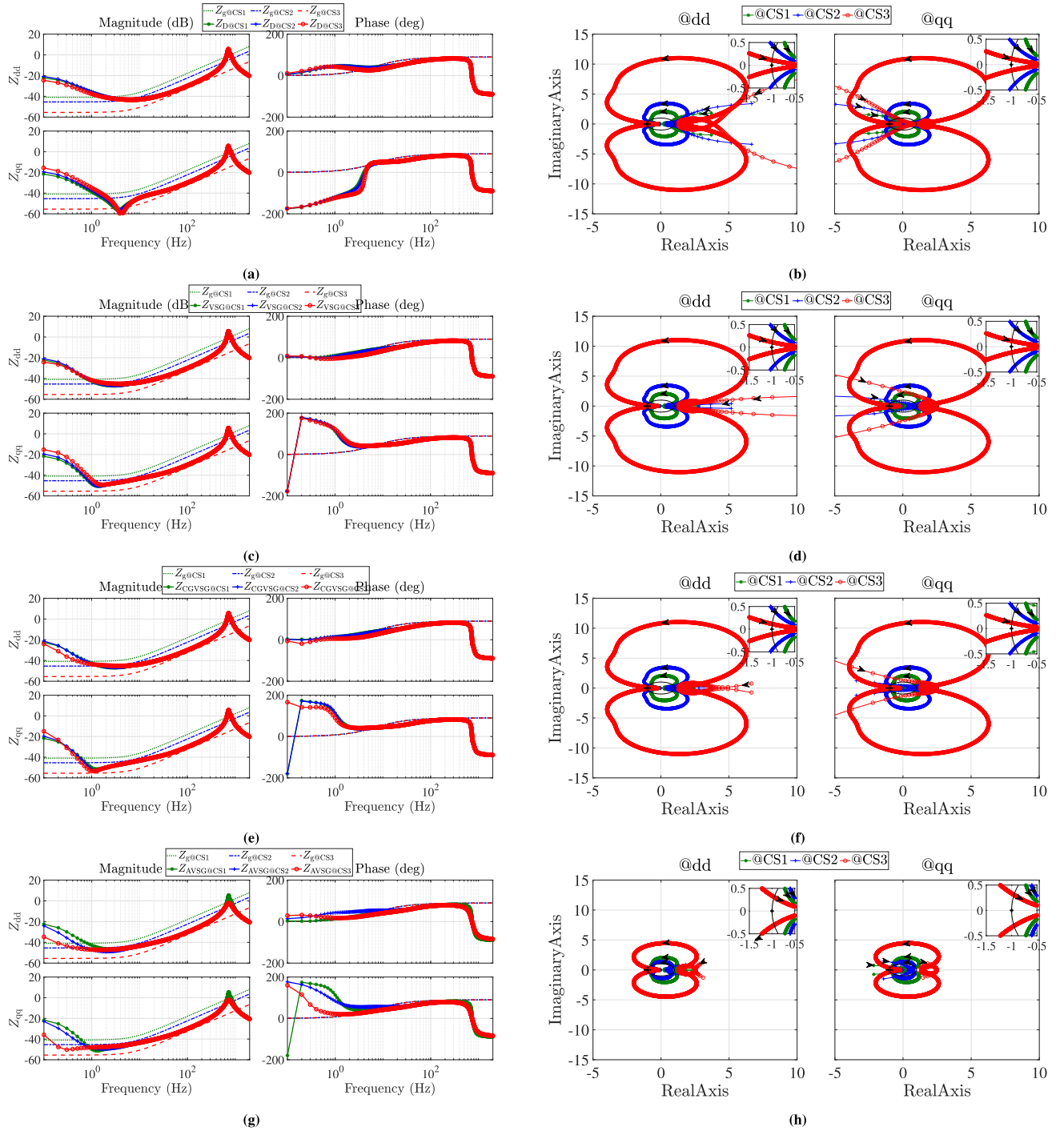


**FIGURE 4.** Impacts of variations in the grid SCR on (left)  $dq$  output impedances of the GFMI and (right) the stability assessment based on the Nyquist criterion for these GFMI when they operate at unity power factor with reference values of  $P_{ref} = 1$  p.u. and  $Q_{ref} = 0$  p.u. CS1, CS2, and CS3 correspond to the GFMI connections to different grids with SCR values of 1.5, 2.5, and 8, respectively. All the cases maintain the same  $X_g/R_g$  ratio of 7. (a) and (b) Droop-based GFMI. (c) and (d) VSG-based GFMI. (e) and (f) CGVSG-based GFMI. (g) and (h) AVSG-based GFMI.

of 8. Unity power factor operation is also maintained with power reference values of  $P_{ref} = 1$  p.u. and  $Q_{ref} = 0$  p.u.

As depicted in Fig. 5(a), variations in  $X_g/R_g$  are found to have a slight impact on the magnitudes and phases of  $Z_{dd}$  and  $Z_{qq}$  of the droop-based GFMI at low frequencies. The

increased influences of  $X_g/R_g$  variations on the root loci of impedance ratios  $Z_{dd}/Z_{gdd}$  and  $Z_{qq}/Z_{gqq}$  are unveiled by the Nyquist plots in Fig. 5(b), with a decrease in the grid  $X_g/R_g$  ratio highlighted by the red curve representing the strong grid scenario. This impact is further verified through time-domain

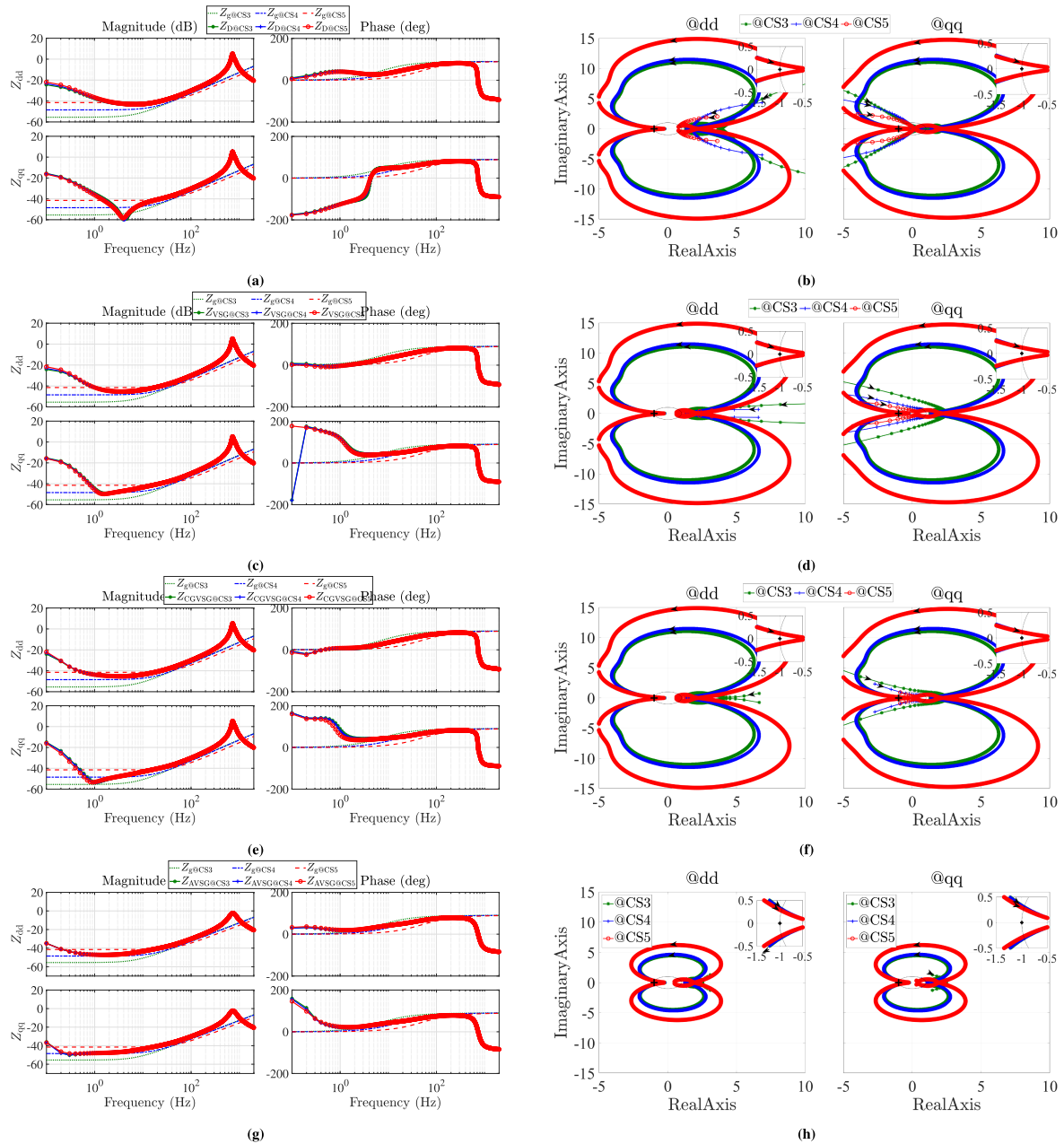


**FIGURE 5.** Impacts of variations in the grid  $X_g/R_g$  on (left)  $dq$  output impedances of the GFMI and (right) the stability assessment based on the Nyquist criterion for these GFMI when they operate at unity power factor with reference values of  $P_{ref} = 1$  p.u. and  $Q_{ref} = 0$  p.u. CS3, CS4, and CS5 correspond to GFMI connections to different grids with  $X_g/R_g$  values of 7, 3, and 1, respectively. All the cases maintain the same SCR of 8. (a) and (b) Droop-based GFMI. (c) and (d) VSG-based GFMI. (e) and (f) CGVSG-based GFMI. (g) and (h) AVSG-based GFMI.

analysis in Fig. 11, where a slight increase in overshoot during the transient response of the droop-based GFMI is observed with a reduced grid  $X_g/R_g$ .

Similar trends are observed in the VSG-based GFMI, as indicated by the Bode and Nyquist plots in Fig. 5(c) and (d), respectively. Notably, increased variations in root loci for  $X_g/R_g$  of 1 indicate less stable operation in comparison to ratios of 7 and 3. These observations are further confirmed by the time-domain simulations in Fig. 11, revealing a degradation in transient response characterized by increased overshoot and extended settling time with small  $X_g/R_g$  values.

Furthermore, the stability of the CGVSG-based system, as illustrated in Fig. 5(e) and (f), and the stability of the AVSG-based GFMI, as depicted in Fig. 5(g) and (h), are similarly affected by the decrease in  $X_g/R_g$ . Such variations are noticed in  $Z_{dd}$  and  $Z_{qq}$  for the CGVSG, especially in the phase of  $Z_{qq}$  when connected to the resistive grid. The extended path of root loci in the resistive grid scenario (CS5), as presented in Fig. 5(f) and (h) for both  $Z_{dd}$  and  $Z_{qq}$ , introduces slight alterations in the step response of both CGVSG- and AVSG-based GFMI, aligning with the observations in the time-domain analysis in Fig. 11.

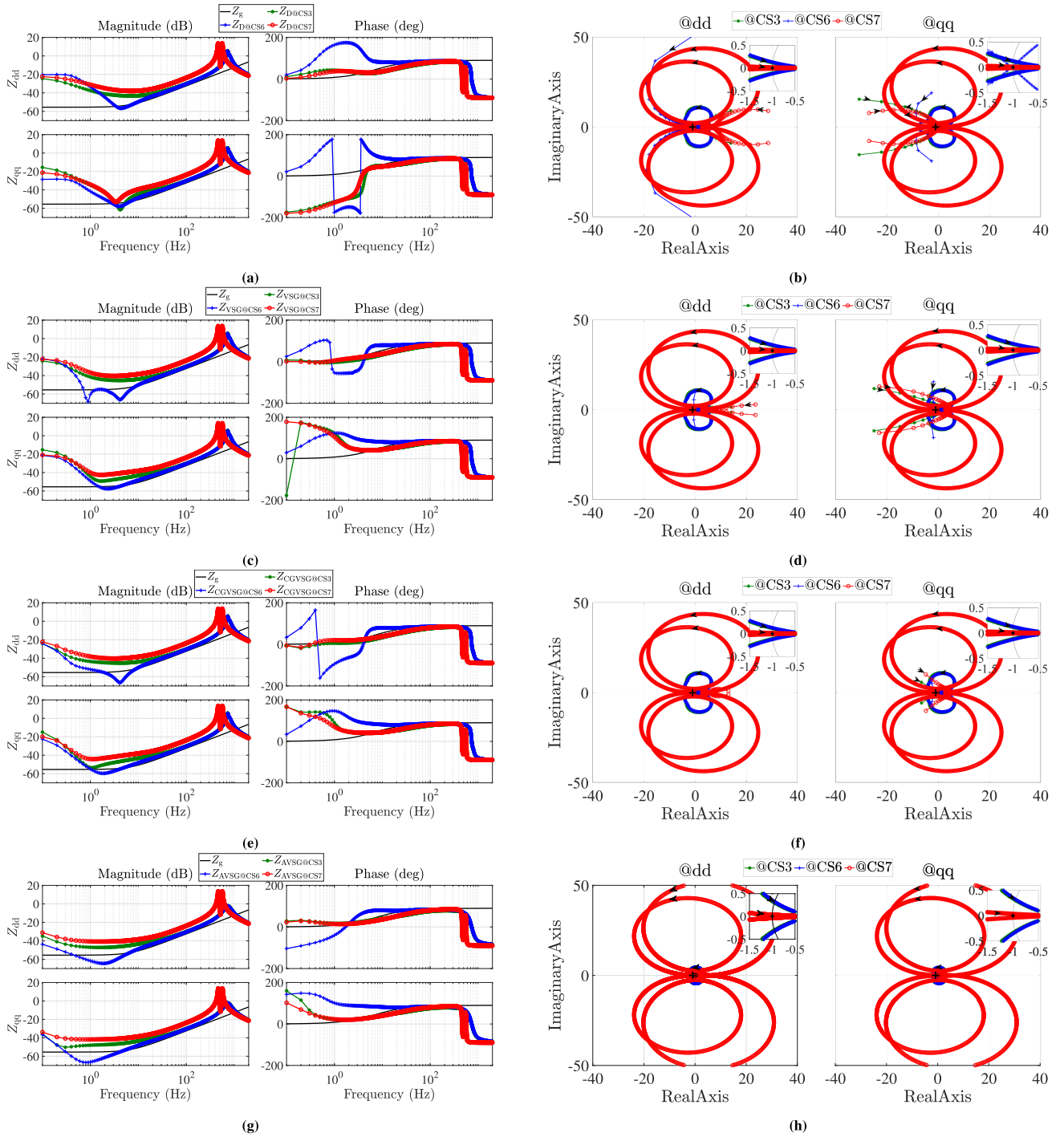


**FIGURE 6.** Impacts of  $Z_{vir}$  and the inner voltage and current loops on (left)  $dq$  output impedances of the GFMI and (right) the stability assessment based on the Nyquist criterion for the four GFMI are examined. In CS3, both  $Z_{vir}$  and inner loops are utilized. In CS6,  $Z_{vir}$  is omitted, but inner loops are retained. In CS7, both  $Z_{vir}$  and inner loops are omitted. All the cases maintain the same SCR of 8 and  $X_g/R_g$  of 7 and operate at unity power factor with reference values of  $P_{ref} = 1$  p.u. and  $Q_{ref} = 0$  p.u. (a) and (b) Droop-based GFMI. (c) and (d) VSG-based GFMI. (e) and (f) CGVSG-based GFMI. (g) and (h) AVSG-based GFMI.

### 3) IMPACT OF $Z_{vir}$ AND INNER LOOPS OF GFMI

The stability investigation of GFMI is carried out here with a focus on the impact of  $Z_{vir}$  and the inner voltage and current loops (see Fig. 6). Three case studies are conducted: CS3, with both  $Z_{vir}$  and inner loops; CS6, without  $Z_{vir}$  but with

inner loops; and CS7, without both  $Z_{vir}$  and inner loops. The grid SCR and  $X_g/R_g$  are held constant at 8 and 7, respectively. Operation at unity power factor with reference values of  $P_{ref} = 1$  p.u. and  $Q_{ref} = 0$  p.u. is also maintained for the three case studies.



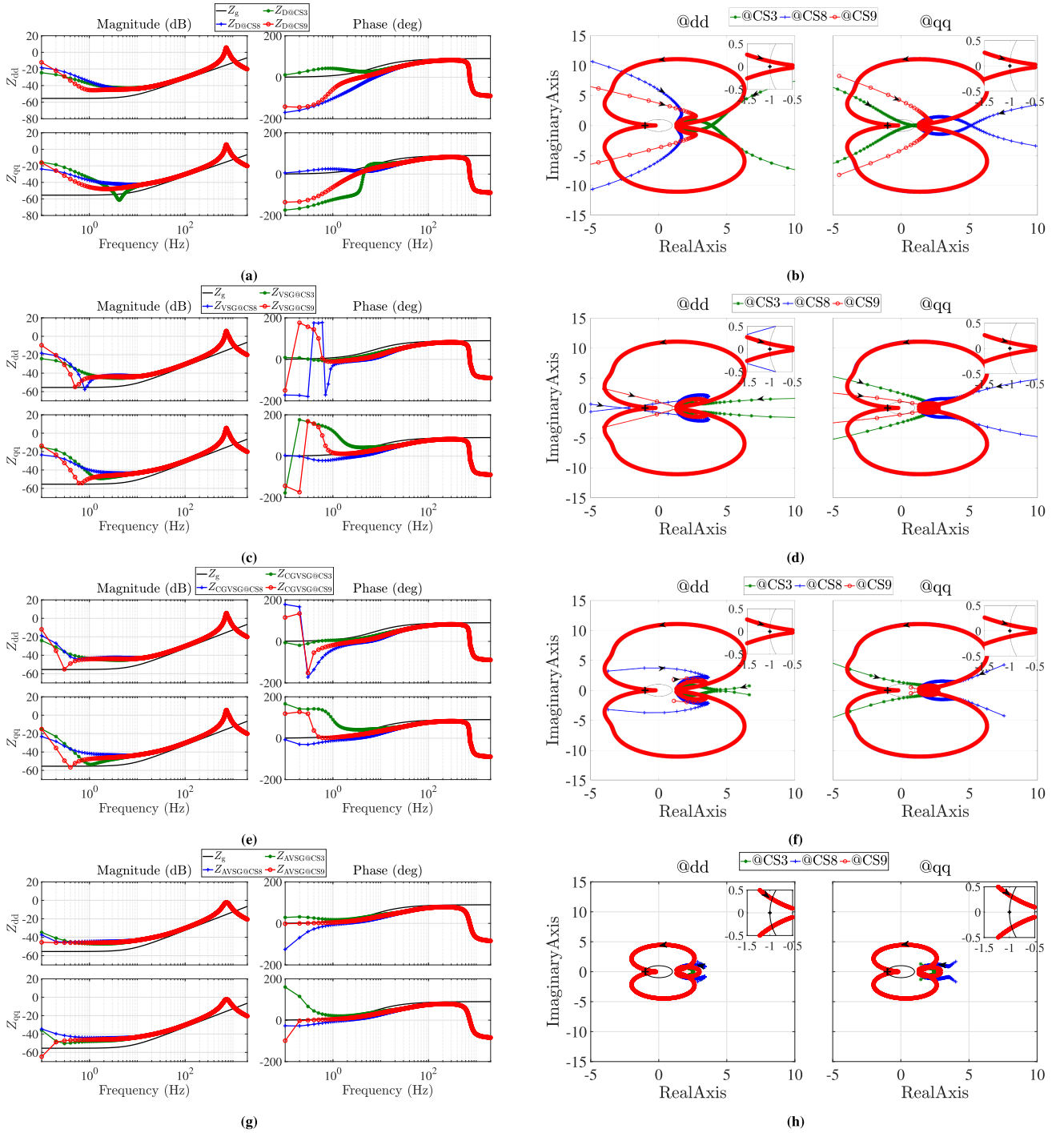


**FIGURE 7.** (Left)  $dq$  output impedance of the GFMI and (right) the stability assessment based on the Nyquist criterion for the GFMI when operating at unity power factor  $Q_{ref} = 0$ . CS3, CS8, and CS9 correspond to the inverter operation at  $P_{rated}$ ,  $-P_{rated}$ , and 0, respectively, all when the inverter is connected to a strong and inductive grid with  $SCR = 8$  and  $X_g/R_g = 7$ . (a) and (b) Droop-based GFMI. (c) and (d) VSG-based GFMI. (e) and (f) CGVSG-based GFMI. (g) and (h) AVSG-based GFMI.

Fig. 6 demonstrates that in all four control techniques of GFMI, the stability is significantly affected by the absence of the virtual impedance and/or the inner voltage and current loops. These effects are manifested in notable variations in the magnitudes and phases of  $Z_{dd}$  and  $Z_{qq}$  in the Bode plots of the output impedances of the inverters, as well as in the root loci

of the impedance ratios  $Z_{dd}/Z_{gdd}$  in the Nyquist plots for all inverters.

In summary, the impacts can be succinctly summarized as follows: in the frequency range  $> 500$  Hz, CS7 exhibits distinct characteristics compared to CS3 and CS6, which share similarities. In the frequency range  $< 100$  Hz, CS3

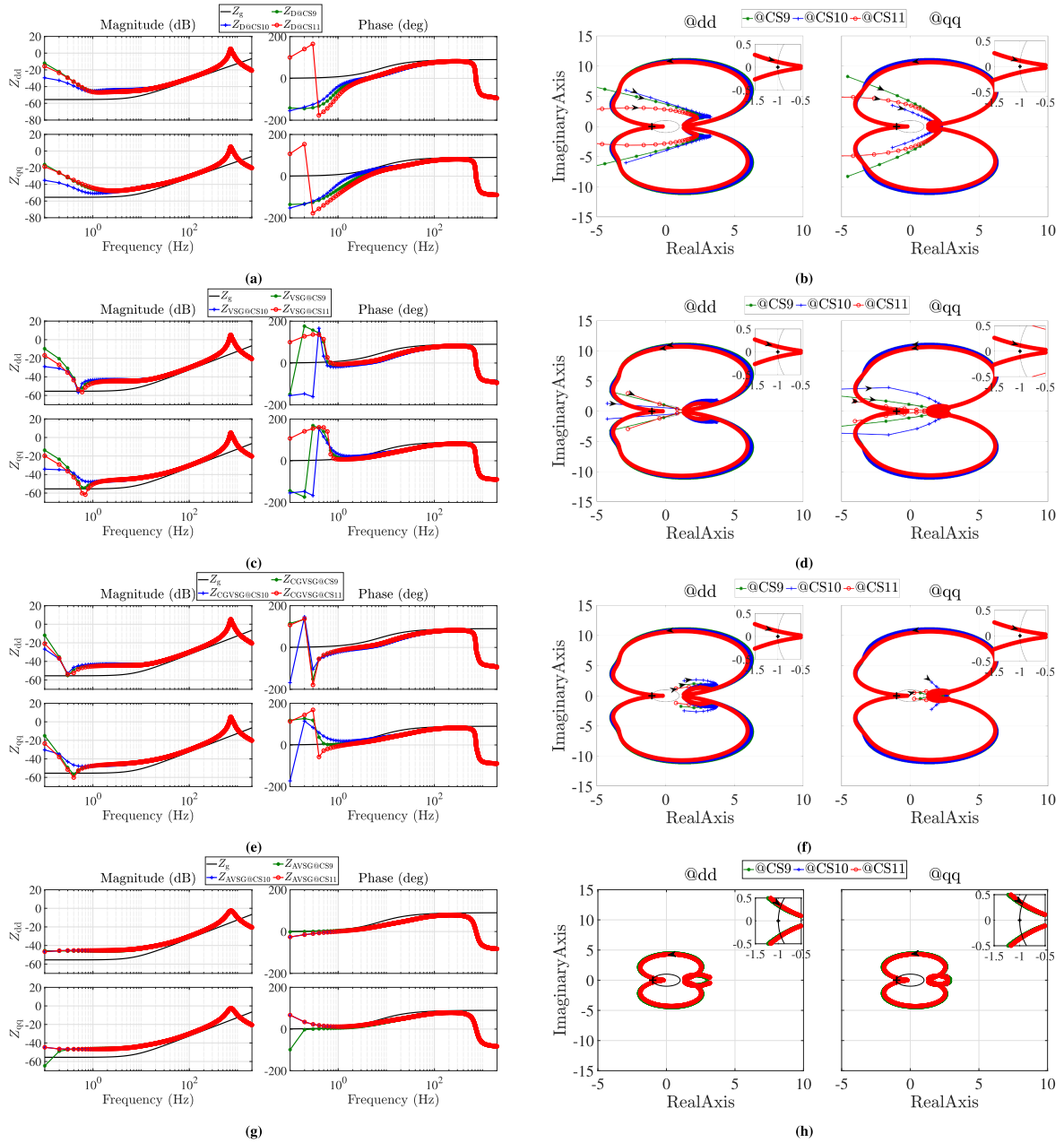


**FIGURE 8.** (Left)  $dq$  output impedance of the GFMI and (right) the stability assessment based on the Nyquist criterion for the GFMI when operating at  $P_{\text{ref}} = 0$ . CS9, CS10, and CS11 correspond to the inverter operation at 0,  $-Q_{\text{rated}}$ , and  $Q_{\text{rated}}$ , respectively, all when the inverter is connected to a strong and inductive grid with  $\text{SCR} = 8$  and  $X_g/R_g = 7$ . (a) and (b) Droop-based GFMI. (c) and (d) VSG-based GFMI. (e) and (f) CGVSG-based GFMI. (g) and (h) AVSG-based GFMI.

and CS7 display similar patterns but differ significantly from CS6. Notably, CS6, operating without  $Z_{\text{vir}}$  yet retaining the inner voltage and current loops, emerges as the less operationally stable case, particularly for the droop- and VSG-based GFMI. This is evidenced by pronounced variations in output impedance magnitude and phase, as well as root loci in the low-frequency range.

These frequency-domain findings are in alignment with time-domain simulations, as seen in Fig. 12. Specifically, the most significant deterioration in the dynamic performance of the droop-based GFMI is experienced in the case of CS6,

characterized by the highest overshoot, oscillations, and the longest settling time of approximately 1 s. Similar results with high overshoot and/or specific oscillations are observed during the step response tests of the other controllers, as shown in  $i_{\text{VSG2}}$ ,  $i_{\text{CGVSG2}}$ , and  $i_{\text{AVSG2}}$ .

#### 4) IMPACT OF ACTIVE POWER REFERENCE VARIATIONS OF GFMI

In this section, the investigation of GFMI stability is conducted with a particular focus on the variation of the inverter operating point, specifically the impact of  $P_{\text{ref}}$  variations.

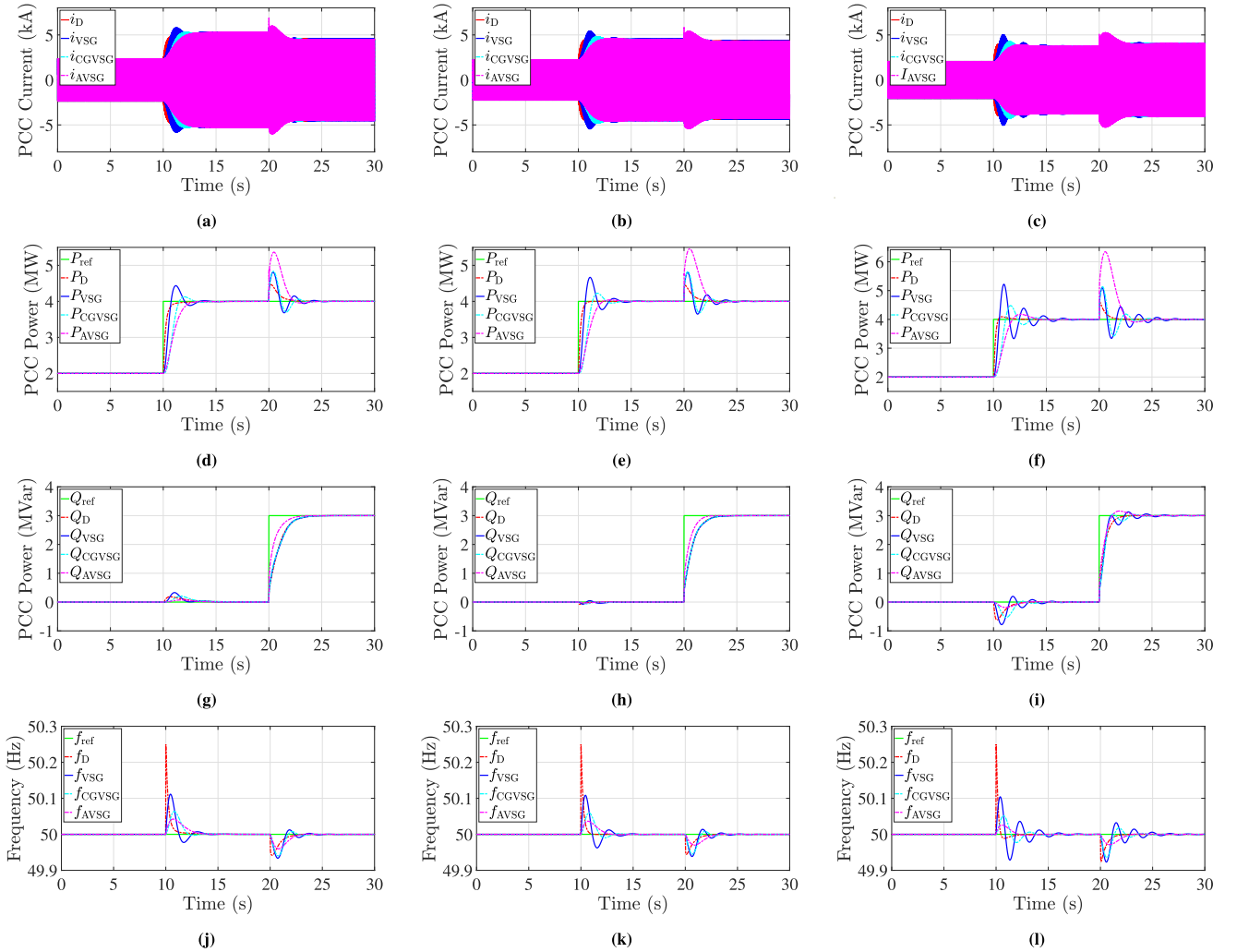


**FIGURE 9.** Performance of the GFMI in weak grids ( $SCR = 1.5$ ) with different  $X_g/R_g$ : (left)  $X_g/R_g = 7$ , (middle)  $X_g/R_g = 3$ , and (right)  $X_g/R_g = 1$ . (a)–(c) PCC current. (d)–(f) PCC active power. (g)–(i) PCC reactive power. (j)–(l) Frequency of the GFMI.

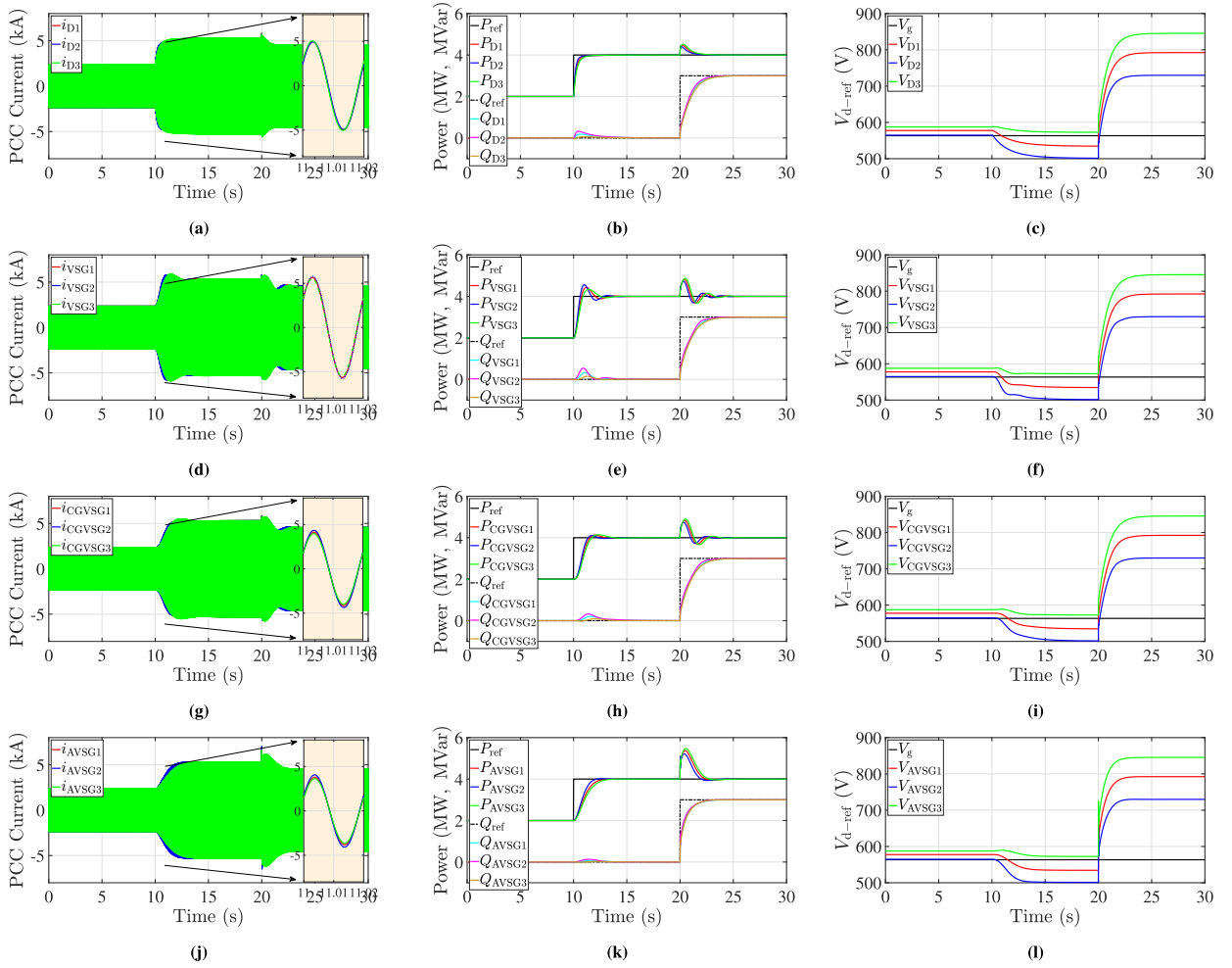
Three distinct case studies, denoted as CS3, CS8, and CS9, are undertaken, corresponding to  $P_{ref}$  values of 1,  $-1$ , and 0 p.u., respectively. Throughout these case studies, the grid SCR, grid ( $X_g/R_g$ ), and  $Q_{ref}$  are held constant at  $SCR = 7$ ,  $X_g/R_g = 8$ , and  $Q_{ref} = 0$  p.u., respectively.

Fig. 7(a), (c), (e), and (g) depicts the Bode plots of  $Z_{dd}$  and  $Z_{qq}$  for the droop-, VSG-, CGVSG-, and AVSG-based GFMI, respectively. The impacts of  $P_{ref}$  variations on the magnitudes and phases of  $Z_{dd}$  and  $Z_{qq}$  can be summarized as follows. On the one hand, variations of  $P_{ref}$  operating point do not affect the impedance at high frequencies, neither the magnitude nor the phase, for all four control techniques of GFMI. On the other hand,  $P_{ref}$  variations have significant impacts on the impedance at low frequencies, especially below 50 Hz, indicating the potential for subsynchronous oscillations under specific operating conditions. This impact is prominently reflected in phase variations of  $Z_{dd}$  and  $Z_{qq}$ . For example, Fig. 7(a) illustrates an approximately  $180^\circ$  phase difference of the droop-based GFMI between CS3 and CS8. A similar analysis is conducted for the VSG and CGVSG, with both

controllers being sensitive to  $P_{ref}$  variations. Interestingly, compared to its counterparts, Fig. 7(g) shows that both  $Z_{dd}$  and  $Z_{qq}$  of the AVSG-based GFMI are relatively less affected by variations in  $P_{ref}$  operating point, indicating the robustness of the AVSG to  $P_{ref}$  variations.

Fig. 7(b), (d), (f), and (h) displays the Nyquist plots of  $dd$  and  $qq$  for the droop-, VSG-, CGVSG-, and AVSG-based GFMI, respectively. Overall, variations in  $P_{ref}$  that result in magnitude and phase changes in  $Z_{dd}$  and  $Z_{qq}$  have an impact on the root locus paths of Nyquist plots for all four control techniques of GFMI. On the one hand, the Nyquist plots vary significantly for the droop-, VSG-, and CGVSG-based GFMI. These effects are manifested in substantial alterations to the root locus trajectories, including changes in their directions and the expansion of the root locus paths in Nyquist plots. On the other hand, Fig. 7(h) confirms the robustness of the AVSG-based GFMI in terms of minor alterations to the root locus trajectories and changes in their directions.

The verification of the stability of the controllers of GFMI in response to variations in  $P_{ref}$  is evident from the conducted



**FIGURE 10.** Performance of the GFMI in a weak and inductive grid with  $SCR = 1.5$  and  $X_g/R_g = 7$  in three cases (1: with  $Z_{vir}$  and with inner loops, 2: without  $Z_{vir}$  and with inner loops, and 3: without  $Z_{vir}$  and without inner loops): (Row 1) droop-based GFMI, (Row 2) VSG-based GFMI, (Row 3) CGVSG-based GFMI, and (Row 4) AVSG-based GFMI.

time-domain results for both weak and strong grids. This assessment is carried out during  $P_{ref}$  step changes occurring at 10 s, as depicted in Figs. 9 and 11 for weak and strong grids, respectively.

#### 5) IMPACT OF REACTIVE POWER REFERENCE VARIATIONS OF GFMI

This section investigates the impact of variations  $Q_{ref}$  on the stability of GFMI. Three distinct case studies, denoted as CS9, CS10, and CS11, are conducted, corresponding to different values for  $Q_{ref}$ : 0,  $-1$ , and 1 p.u. Throughout these case studies, the grid  $SCR$ , grid  $X_g/R_g$ , and  $P_{ref}$  are kept constant at  $SCR = 7$ ,  $X_g/R_g = 8$ , and  $P_{ref} = 0$  p.u., respectively.

Fig. 8(a), (c), (e), and (g) depicts Bode plots of  $Z_{dd}$  and  $Z_{qq}$  for the droop-, VSG-, CGVSG-, and AVSG-based GFMI, respectively. Similar to the variations in  $P_{ref}$ , it is observed that variations in  $Q_{ref}$  do not impact the magnitudes and phases of  $Z_{dd}$  and  $Z_{qq}$  at high frequencies. However, they do have an impact at low frequencies, especially below 50 Hz. For instance,

the phases of impedances for the droop-, VSG-, and CGVSG-based GFMI vary significantly, approaching almost  $360^\circ$ . Furthermore, the AVSG-based GFMI demonstrates greater robustness to variations in  $Q_{ref}$  with only minimal variations in both magnitude and phase of  $Z_{dd}$  and  $Z_{qq}$ .

Fig. 8(b), (d), (f), and (h) displays the corresponding Nyquist plots of  $dd$  and  $qq$  for these four control techniques of GFMI, respectively. It is clear that the root locus trajectories of the droop-, VSG-, and CGVSG-based GFMI are significantly influenced by the variations in  $Q_{ref}$ . However, Fig. 8(h) confirms the robustness of the AVSG-based GFMI under such operating conditions.

The assessment of controller stability for GFMI under varying  $Q_{ref}$  is confirmed in the time domain for both weak and strong grids, as illustrated in Figs. 9 and 11, respectively.

#### IV. TIME-DOMAIN SIMULATIONS

To further validate the dynamic performance characteristics unveiled through the small-signal analysis in the frequency domain, a comprehensive time-domain analysis of the droop,



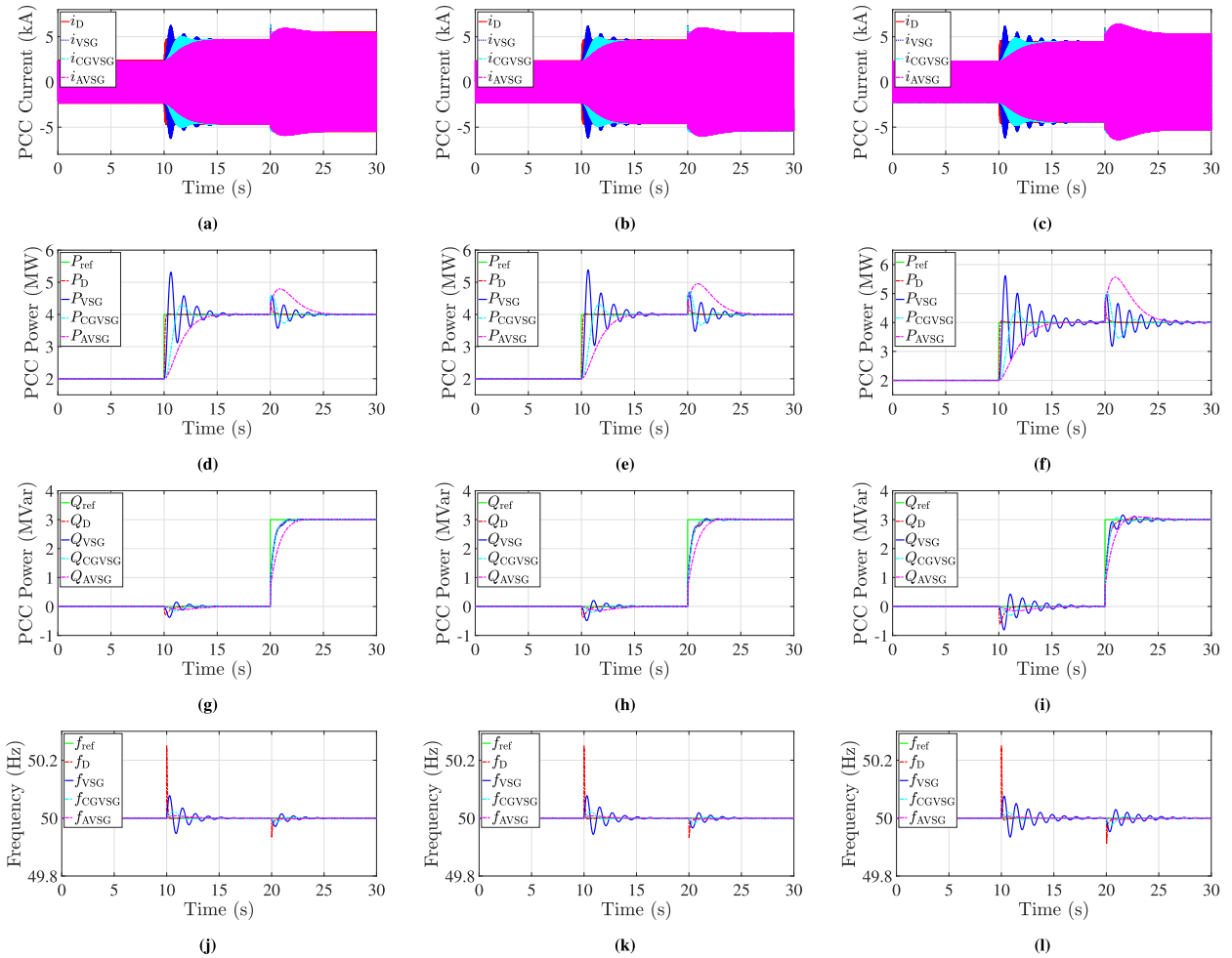


**FIGURE 11.** Performance of the GFMI in strong grids ( $SCR = 8$ ) with different  $X_g/R_g$  (left)  $X_g/R_g = 7$ , (middle)  $X_g/R_g = 3$ , and (right)  $X_g/R_g = 1$ . (a)–(c) PCC current. (d)–(f) PCC active power. (g)–(i) PCC reactive power. (j)–(l) Frequency of the GFMI.

VSG, CGVSG, and AVSG is presented in this section. The block diagrams depicted in Figs. 1 and 2 are simulated within the MATLAB/Simulink environment considering a range of testing scenarios. The parameters employed for the simulation study are detailed in Table 1.

The evaluation of these controllers considers the operation in both weak and strong grid scenarios. Within each operational condition, assessments are made regarding responses to changes in active and reactive power commands. Furthermore, for both grid conditions, the effect of the virtual impedance and the inner control loops on system performance is explored.

## A. WEAK GRID

The performance of the droop-, VSG-, CGVSG-, and AVSG-based GFMI in the weak grid with an SCR value of 1.5 is presented in this section as follows.

### 1) RESPONSE TO STEP CHANGE IN POWER REFERENCES

The dynamic response of the controllers is evaluated by applying step changes to active and reactive power references.

Initially, steady-state conditions are maintained with active power and reactive power references set to  $P_{ref} = 2$  MW and  $Q_{ref} = 0$  MVar, respectively, for all four controllers. Subsequently, a step change is introduced in active power to  $P_{ref} = 4$  MW at 10 s, followed by a reactive power change up to  $Q_{ref} = 3$  MVar at 20 s. The PCC currents, active and reactive powers, and internal frequency waveforms under this testing condition are depicted in Fig. 9. The responses of all considered controllers are concurrently plotted in the same graphs to seamlessly highlight the differences in performance between these control methods.

As illustrated in Fig. 9(d)–(i), all four controllers effectively track the active and reactive power references, exhibiting zero steady-state error regardless of the  $X_g/R_g$  ratio. Nonetheless, it is notable that the VSG's power tracking performance demonstrates more oscillations at lower  $X_g/R_g$  ratios compared to the other controllers. Specifically, at  $X_g/R_g = 1$ , the VSG exhibits a settling time exceeding 5 s in active power tracking, accompanied by higher power swing peaks compared to the other controllers, as evident in Fig. 9(f). In addition, the AVSG displays a notable coupling between active and reactive

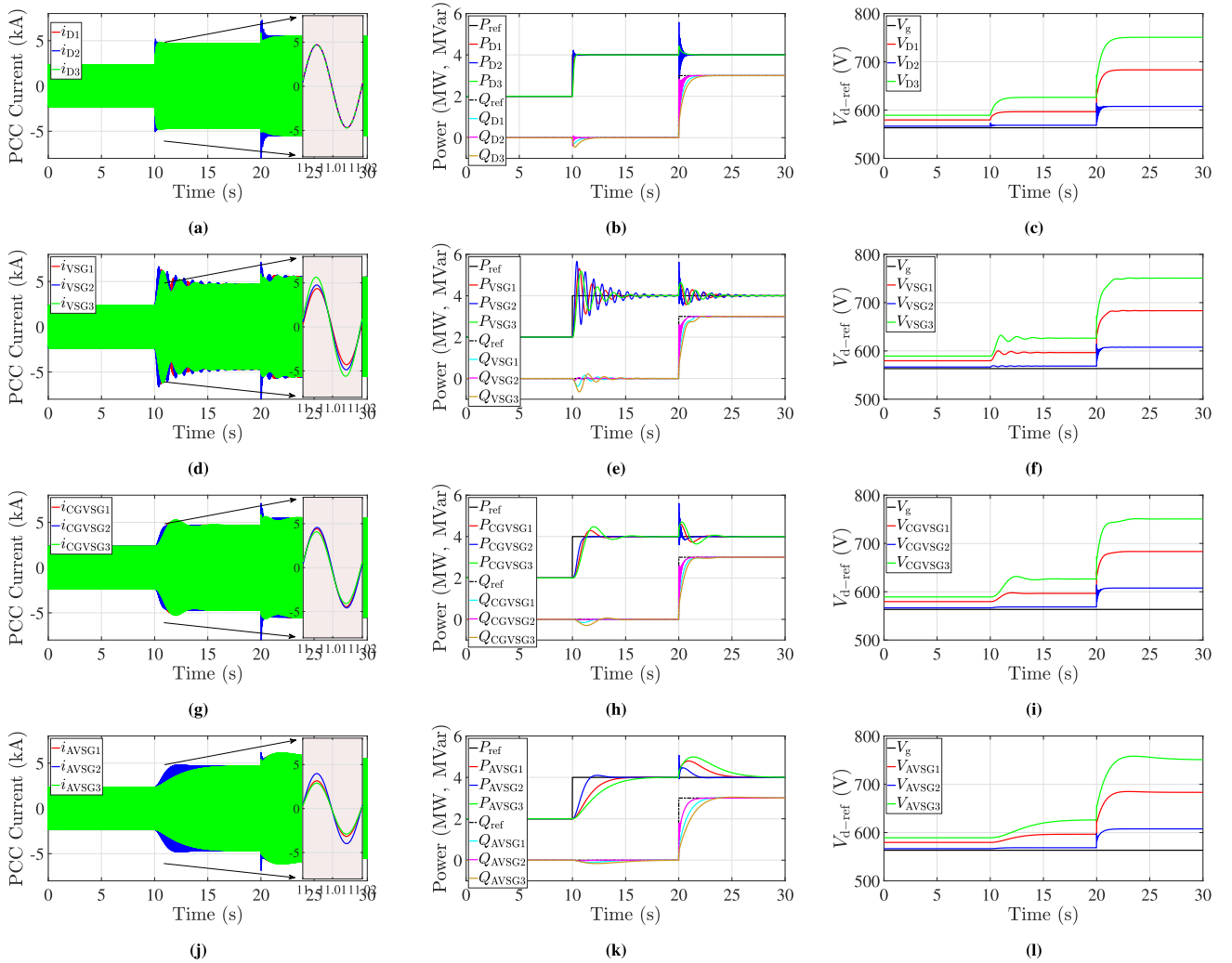


**FIGURE 12.** Performance of the GFMI in a strong and inductive grid with  $SCR = 8$  and  $X_g/R_g = 7$  in three cases (1: with  $Z_{vir}$  and with inner loops, 2: without  $Z_{vir}$  and with inner loops, and 3: without  $Z_{vir}$  and without inner loops): (Row 1) droop-based GFMI, (Row 2) VSG-based GFMI, (Row 3) CGVSG-based GFMI, and (Row 4) AVSG-based GFMI.

powers, evidenced by a pronounced overshoot in the active power waveform at 20 s when subjected to a reactive power step change, as depicted in Fig. 9(d)–(f). In the most extreme case, despite maintaining stability and achieving a settling time of approximately 3 s, the AVSG exhibits an overshoot exceeding 6 MW for  $X_g/R_g = 1$ . Notably, all controllers effectively track the reactive power change with minimal or no overshoot, as demonstrated in Fig. 9(g)–(i).

Fig. 9(j)–(l) depicts the internal frequency generated by each controller. It is evident that the droop exhibits sharp peaks at 10 and 20 s due to the absence of inertia. Although the droop settles back to the steady-state frequency value much faster than the other controllers, this extremely high RoCoF is deemed unacceptable in a power system. Such a RoCoF could potentially trigger RoCoF-sensitive relays or damage RoCoF-sensitive equipment [28]. On the other hand, less RoCoF is observed in the other three controllers. While the VSG experiences frequency swings that can last up to 5 s,

the CGVSG provides a good tradeoff as it possesses faster and more damped dynamic responses under step changes of active and reactive power reference commands, as well as a low RoCoF during power reference changes. Finally, the AVSG outperforms other controllers in exhibiting better robustness in frequency response, especially under step changes of reactive power reference command.

## 2) IMPACT OF $Z_{vir}$ AND INNER LOOPS

This section investigates the impacts of  $Z_{vir}$  and the inner loop dynamics on performance in weak grid connections. The PCC current, active power, and voltage waveforms are depicted in Fig. 10 under three case studies: with virtual impedance and inner loops (Case 1), without virtual impedance and with inner loops (Case 2), and without both virtual impedance and inner loops (Case 3).  $Z_{vir}$  is placed between the primary controller and the inner voltage controller, as illustrated in Fig. 1. The value assigned to  $Z_{vir}$  in this study is detailed in Table 1.

Furthermore, the inner loops, referring to the inner current and voltage control loops, are bypassed in Case 3, and the outputs of the primary controller are directly fed into the PWM signal generator.

Initially, all four controllers are in a steady-state condition, with active power and reactive power references set at  $P_{\text{ref}} = 2$  MW and  $Q_{\text{ref}} = 0$  MVar, respectively. Subsequently, a step change is introduced in the active power reference, raising it to  $P_{\text{ref}} = 4$  MW at 10 s, followed by a reactive power change to  $Q_{\text{ref}} = 3$  MVar at 20 s. The grid  $X_g/R_g$  is maintained at a fixed value of 7 throughout the test.

Fig. 10(a), (d), (g), and (j) highlights slight variations in the PCC current waveforms during the transient period commencing at 10 s. As depicted in Fig. 10(b) and (h), similar dynamic responses in terms of active and reactive power tracking are exhibited by the droop and the CGVSG, regardless of the presence or absence of virtual impedance and inner loops. Fig. 10(e) illustrates that in the case of the VSG, the absence of  $Z_{\text{vir}}$  notably degrades the decoupling performance, as indicated by a slightly higher peak at 20 s in the active power trace. This degradation is similarly evident in other controllers, with a maximum peak of just under 5 MVar. A faster response is observed in Case 2 by the AVSG, while slower yet well-damped responses are demonstrated in Cases 1 and 3 in terms of active power tracking, as depicted in Fig. 10(h). It is worth noting that the rise times in all three cases are nearly identical, with the exception of the AVSG. In the VSG, Case 3 exhibits the lowest overshoot for the active power change at 10 s. In addition, settling times of just under 5 s in active power tracking are observed in all traces for the VSG, notwithstanding slight reductions in the peak amplitude of the oscillation in Cases 2 and 3.

Overall, when considering the  $d$ -axis voltage reference plots in Fig. 10(c), (f), (i), and (l), all the controllers showcase closely similar characteristics. It can be observed that the case without both  $Z_{\text{vir}}$  and inner loops results in the highest voltage shift, reaching around 850 V in a steady state after the reactive power change at 20 s. However, Case 2 has a lower steady-state voltage reference value compared to Case 1, which includes virtual impedance. This voltage difference is caused by the voltage drop created across the virtual impedance (see the virtual impedance block in Fig. 1).

## B. STRONG GRID

In this section, the performance of the four controllers is assessed in a strong grid with an SCR of 8 under the same testing conditions outlined in the weak grid scenario. The outcomes from these specific test scenarios are detailed as follows.

### 1) RESPONSE TO STEP CHANGE IN POWER REFERENCES

To evaluate the dynamic response of the controllers, step changes are induced in both active and reactive power references. Initially, steady-state conditions prevail for all four controllers, with active power and reactive power references

set to  $P_{\text{ref}} = 2$  MW and  $Q_{\text{ref}} = 0$  MVar, respectively. Subsequently, a step change in active power to  $P_{\text{ref}} = 4$  MW at 10 s is followed by a reactive power change to  $Q_{\text{ref}} = 3$  MVar at 20 s. The PCC currents, active and reactive power, and frequency waveform during this testing scenario are illustrated in Fig. 11.

Fig. 11 shows the effective tracking of active and reactive power references by the droop, VSG, CGVSG, and AVSG, with no observable steady-state errors, irrespective of the  $X_g/R_g$  ratio.

The step change in active power to 4 MW at 10 s reveals that the response of the droop exhibits a very small overshoot in the resistive grid compared to the inductive grid, as depicted in Fig. 11(d) and (f). Furthermore, the dynamic performance of the VSG deteriorates notably in strong grids and worsens further in resistive grids as the  $X_g/R_g$  ratio decreases, resulting in highly oscillatory power tracking. This manifests undesirable behavior in the VSG response, as seen in Fig. 11(c), (f), (i), and (l), with an underdamped response persisting for more around 10 s.

The response of the CGVSG and AVSG to this step change in active power at 10 s is shown to be robust, exhibiting almost no changes with a decreasing  $X_g/R_g$  ratio. However, substantial overshoots are noted in the AVSG response at 20 s, reaching a maximum slightly above 6 MW when the  $X_g/R_g$  ratio is at its lowest value, as illustrated in Fig. 11(f). Consequently, the current at the PCC experiences higher transient behavior, showcasing undesirable coupling between active and reactive power.

Furthermore, when examining the frequency dynamics, a pronounced peak at 10 s is observed in the case of the droop, where an almost 50.25 Hz is reached. An oscillatory response, characterized by reduced overshoots and an extended settling time of nearly 5 and 10 s, is exhibited by the VSG in inductive and resistive grids, respectively. Notably, a much deeper sudden decrease in frequency of the droop to approximately 49.9 Hz at 20 s is induced by the step change in reactive power, as depicted in Fig. 11(j)–(l), when compared to the other three controllers. In summary, robust and more damped dynamic responses are demonstrated by the CGVSG and the AVSG under step changes in active and reactive power reference commands, resulting in a lower RoCoF during power reference adjustments.

### 2) IMPACT OF $Z_{\text{VIR}}$ AND INNER LOOPS

This section investigates the impact of virtual impedance implementation or inner loop dynamics removal on performance in the strong grid case with an SCR of 8. Fig. 12 presents the PCC current, active power, and voltage waveforms for three case studies: Case 1 involves the utilization of both virtual impedance and inner loops, Case 2 employs inner loops without virtual impedance, and Case 3 eliminates both virtual impedance and inner loops. It is noteworthy that the value of  $Z_{\text{vir}}$  remains constant, aligned with the conditions established in the weak grid case.

Similarly, as in the weak grid case, all four controllers are initially operated in a steady state, with the active power and reactive power references set to  $P_{\text{ref}} = 2$  MW and  $Q_{\text{ref}} = 0$  MVar, respectively. Subsequently, at 10 s, a step change in the active power reference,  $P_{\text{ref}} = 4$  MW, is introduced, followed by a subsequent reactive power change to  $Q_{\text{ref}} = 3$  MVar at 20 s. In the three cases, the  $X_g/R_g$  ratio is kept constant at a value of 7.

As illustrated in Fig. 12(a)–(c), relatively similar dynamic responses are observed in the droop for both Cases 1 and 3, particularly with regard to the response to active power variations. However, the absence of  $Z_{\text{vir}}$  noticeably in Case 2 leads to deterioration in the system's dynamic response. This is evidenced by oscillations and substantial peaks, especially at 20 s, in both the active and reactive power traces. Similar issues are observed in the other controllers, with a maximum peak of just under 6 MVar.

In contrast to the weak grid case, the power tracking responses of the three cases are distinct, particularly in the VSG and the AVSG, as illustrated in Fig. 12(e) and (k), respectively. In the VSG, the removal of virtual impedance and the inner control loops in Case 3 is observed to mitigate oscillatory behavior to a certain extent. Nevertheless, the VSG exhibits settling times greater than 5 s in active power tracking, despite slight reductions in the peak amplitude of the oscillation in Cases 1 and 3.

Although almost identical rise times in power tracking are exhibited by the CGVSG, as depicted in Fig. 12(h), a slightly higher overshoot and longer settling times are observed in Case 3, while Case 2 displays a fast-damped yet oscillatory response at 20 s. Notably, the AVSG demonstrates a faster response in Case 2, while performing slower yet well damped in Case 1 with both  $Z_{\text{vir}}$  and inner loops in terms of active power tracking. The longest rise time among the three considered cases in AVSG traces is portrayed in Case 3, reaching almost 5 s.

When examining the  $d$ -axis voltage reference plots in Fig. 12(c), (f), (i), and (l), all the controllers exhibit remarkably similar characteristics. In contrast to the weak grid scenario, none of the controllers allow the  $d$ -axis voltage to drop below the grid voltage ( $V_g$ ) after the active power change at 10 s. Notably, the case without both  $Z_{\text{vir}}$  and inner loops results in the highest steady-state voltage shift, stabilizing at around 750 V after the reactive power change at 20 s. On the other hand, Case 2 presents a lower steady-state voltage reference compared to Case 1, which includes virtual impedance. This voltage disparity is attributed to the voltage drop across the virtual impedance.

## V. EXTERNAL GRID DISTURBANCES

Unlike the results presented in the previous sections, in which the parameters of the grid voltage sources are assumed to be constants and equal to the nominal values listed in Table 1, this section explores the performance of the GFMI in more dynamic and challenging situations.

In this section, the evaluation of the performance of the four control strategies for GFMI is conducted, with a primary focus on their resilience in the face of external grid disturbances. The tests include three critical scenarios involving frequency deviations, phase jumps, and voltage sags, all within the grid voltage sources. To ensure a comprehensive assessment, varying levels of disturbance magnitude are considered for each test. Furthermore, the performance evaluation extends to both weak and strong grid conditions, as detailed below.

### A. WEAK GRID

The performance of the four considered controllers in the weak grid with  $\text{SCR} = 1.5$  is evaluated in this section. The response of each control strategy to external grid disturbances is detailed as follows.

#### 1) FREQUENCY DEVIATION

With the aim of examining how the GFMI respond to grid disturbances, such as generator or load tripping, three distinct frequency deviations are introduced in the grid voltage source during this test. Throughout the test, active and reactive power references are set to  $P_{\text{ref}} = 4$  MW and  $Q_{\text{ref}} = 0$  MVar. Frequency deviations of 0.1, 0.25, and 0.5 Hz are applied at 5 s, as illustrated in Fig. 13(j)–(l), respectively.

In all three scenarios, the effective tracking of grid frequency deviations is demonstrated by all controllers with zero steady-state errors. It is evident that the droop method exhibits the fastest response, characterized by the shortest rise time and zero overshoot, regardless of the magnitude of frequency deviation. When assessing the VSG and the CGVSG, lower overshoots are consistently observed with CGVSG, including in the case of 0.5-Hz frequency deviation. Conversely, the AVSG exhibits longer settling times of more than 5 s with substantial overshoots as the frequency deviation increases to 0.5 Hz. However, the AVSG outperforms other VSG-based controllers when the frequency changes from 50 to 50.1 Hz [see Fig. 13(j)]. In addition, Fig. 13(d)–(f) illustrates how the active power value of the AVSG deviates from the values of the other controllers after frequency deviation. The sensitivity of the AVSG to grid frequency disturbances is attributed to the adaptive tuning of its damping coefficient in real time [29].

#### 2) PHASE JUMP

Similar to the previous test, the active and reactive power references are maintained at  $P_{\text{ref}} = 4$  MW and  $Q_{\text{ref}} = 0$  MVar for this evaluation. Phase jumps of  $15^\circ$ ,  $30^\circ$ , and  $45^\circ$  are introduced at 5 s to the three phases of the grid voltage source, mimicking disturbances in the power system during fault conditions [68].

As depicted in Fig. 14, the controllers exhibit stability across all testing cases following the imposition of phase jumps. Notably, with the exception of the VSG, all other controllers display minimal overshoots and reduced oscillations. The droop system produces severe frequency spikes at 5 s due to the phase jump, attributed to its lack of inertia. In the most



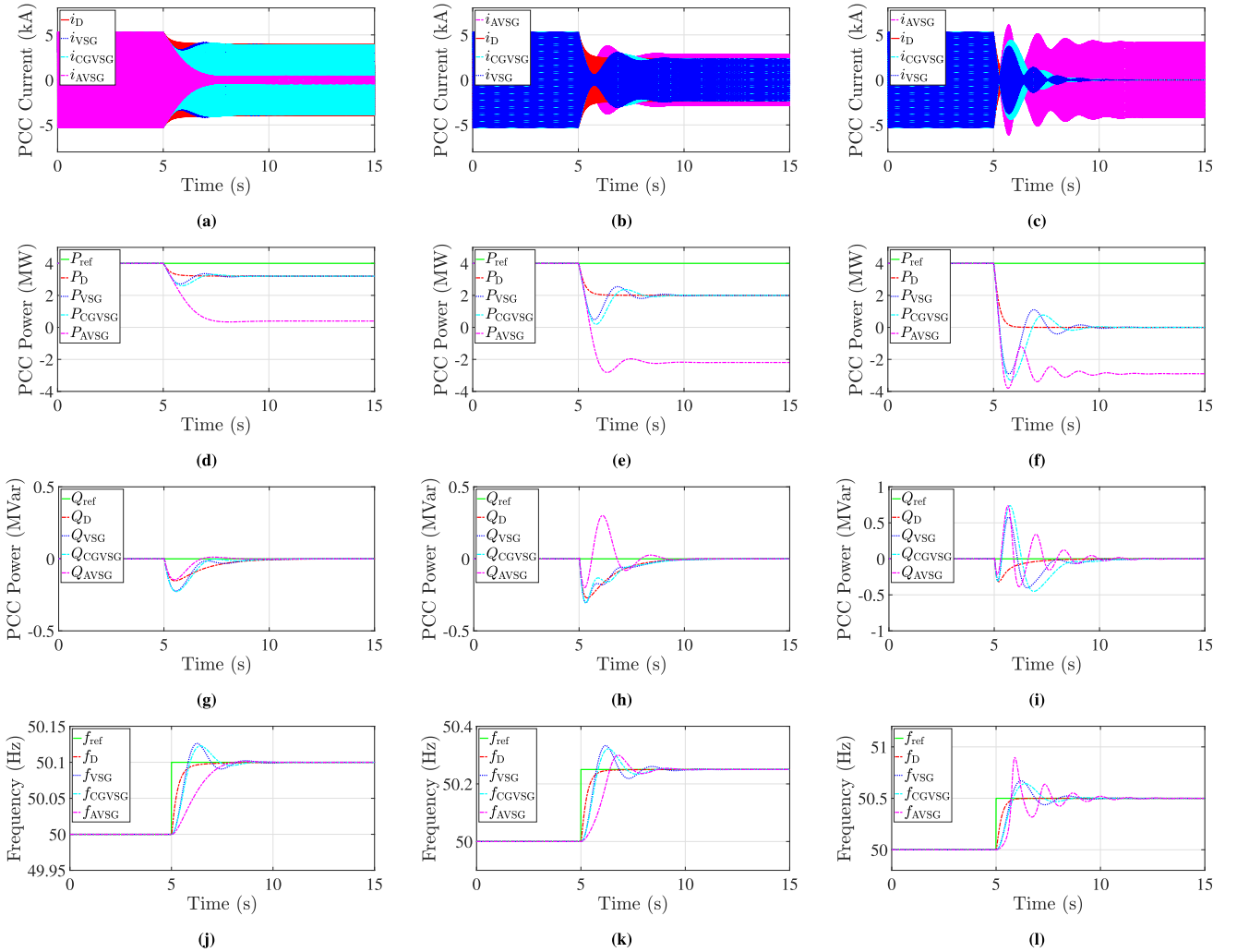


**FIGURE 13.** Performance of the GFMs in a weak grid ( $SCR = 1.5$ ,  $X_g/R_g = 7$ ) under frequency deviations of the grid voltage source (left) 0.1 Hz, (middle) 0.25 Hz, and (right) 0.5 Hz. (a)–(c) PCC current. (d)–(f) PCC active power. (g)–(i) PCC reactive power. (j)–(l) Frequency of the GFMs.

severe instance of the  $45^\circ$  phase jump, the droop frequency reaches just under 50.5 Hz, as illustrated in Fig. 14(l). This frequency spike has the potential to violate the established safe frequency limits in power systems.

Upon evaluating the active power response to the phase jumps, the VSG and the CGVSG exhibit substantial overshoots, contributing to a pronounced transient nature in the PCC current waveform, particularly in the VSG, as shown in Fig. 14(b) and (c). Interestingly, despite its damped behavior, the CGVSG demonstrates a higher RoCoF than the VSG. Conversely, in the analysis of frequency response to the phase jumps, it becomes evident that the AVSG outperforms all other controllers, even in the most challenging scenario of a  $45^\circ$  phase jump, as shown in Fig. 14(f), (i), and (l).

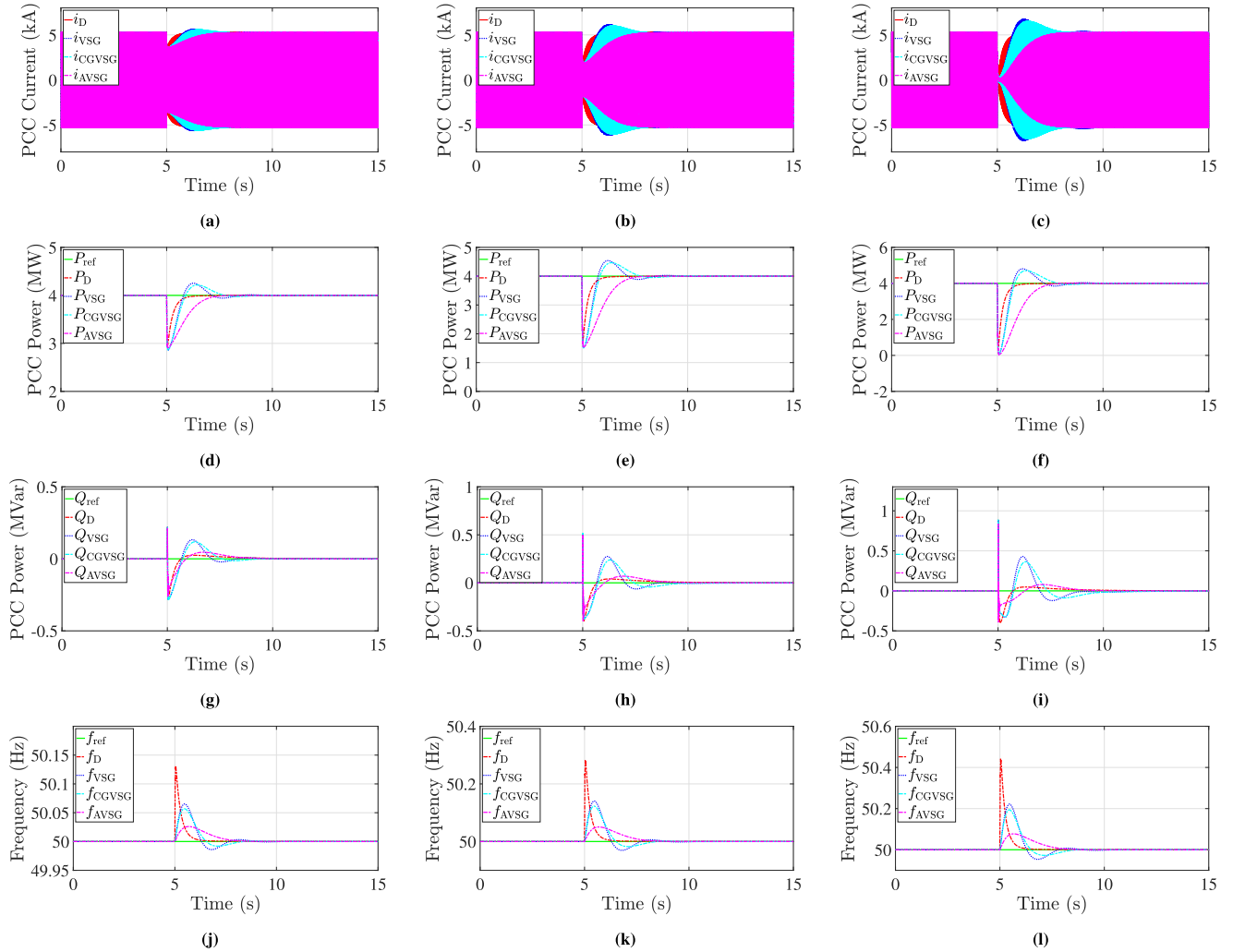
### 3) VOLTAGE SAG

Fig. 15 reveals the system responses under a symmetrical voltage sag applied at 5 s for 200 ms. These voltage sags, which may occur in real power systems due to faults, are considered

at three different levels for this test scenario, and active and reactive power reference commands are kept consistent with the previous two cases.

Robustness is demonstrated by all controllers even against a severe 50% voltage sag, as depicted in Fig. 15(c), (f), (i), and (l), with almost identical settling times. This underscores the GFM capability of these control methods, acting as a voltage source in the absence of support from the main grid. It is observed how reactive power is abruptly increased at 5 s to support the grid during the voltage sag. As expected, the amount of reactive power injected into the grid rises with the severity of the voltage sag. In the case of a 50% voltage sag, as shown in Fig. 15(i), nearly 2 MVar of reactive power is injected by the droop, VSG, and CGVSG. Meanwhile, less reactive power is injected by the AVSG.

Fig. 15(j)–(l) reveals an abrupt rise in the droop frequency when the active power is reduced in response to the grid voltage sag. This high RoCoF behavior aligns with the previous frequency event-triggering cases considered in the



**FIGURE 14.** Performance of the GFMI in a weak grid ( $SCR = 1.5$ ,  $X_g/R_g = 7$ ) under phase jumps of the grid voltage source (left)  $15^\circ$ , (middle)  $30^\circ$ , and (right)  $45^\circ$ . (a)–(c) PCC current. (d)–(f) PCC active power. (g)–(i) PCC reactive power. (j)–(l) Frequency of the GFMI.

time-domain study. However, despite their considerable settling times of approximately 3–4 s, the lowest RoCoF values are exhibited by the VSG, CGVSG, and AVSG.

## B. STRONG GRID

This section demonstrates the performance of the four controllers in the strong grid with  $SCR = 8$  under the same testing conditions described in the weak grid case. The outcomes from these particular test scenarios are as follows.

### 1) FREQUENCY DEVIATION

During the evaluation of controller responses to grid disturbances, three specific frequency deviations are introduced into the grid voltage source. Throughout this analysis, constant references for active and reactive power, set at 4 MW and 0 MVar, respectively, are maintained. The considered frequency deviations of 0.1, 0.25, and 0.5 Hz are applied at 5 s, visually represented in Fig. 16(j)–(l), respectively.

In all three scenarios, the grid frequency changes are adeptly tracked by the droop and CGVSG methods, exhibiting minimal to zero overshoot, thereby underscoring their robustness in the presence of grid disturbances. Conversely, longer settling times exceeding 10 s are observed in the case of AVSG, particularly evident in Fig. 16(l), along with the most significant overshoots. The oscillations in the AVSG are reflected in reactive power responses, reaching almost 2 MVar. Notably, the AVSG effectively tracks the frequency change of 0.1 Hz without oscillations, surpassing the performance of VSG, as depicted in Fig. 16(j). In contrast to the weak grid case, where all controllers display negative peaks in reactive power at the lowest frequency deviation, the AVSG exhibits a positive peak of just under 2 MVar, as depicted in Figs. 13(g) and 16(g). Moreover, the VSG demonstrates considerably prolonged settling times of around 10 s in all three considered cases, despite effectively tracking the frequency change.

Throughout this study, it is crucial to note that the controllers have been deliberately designed without any current

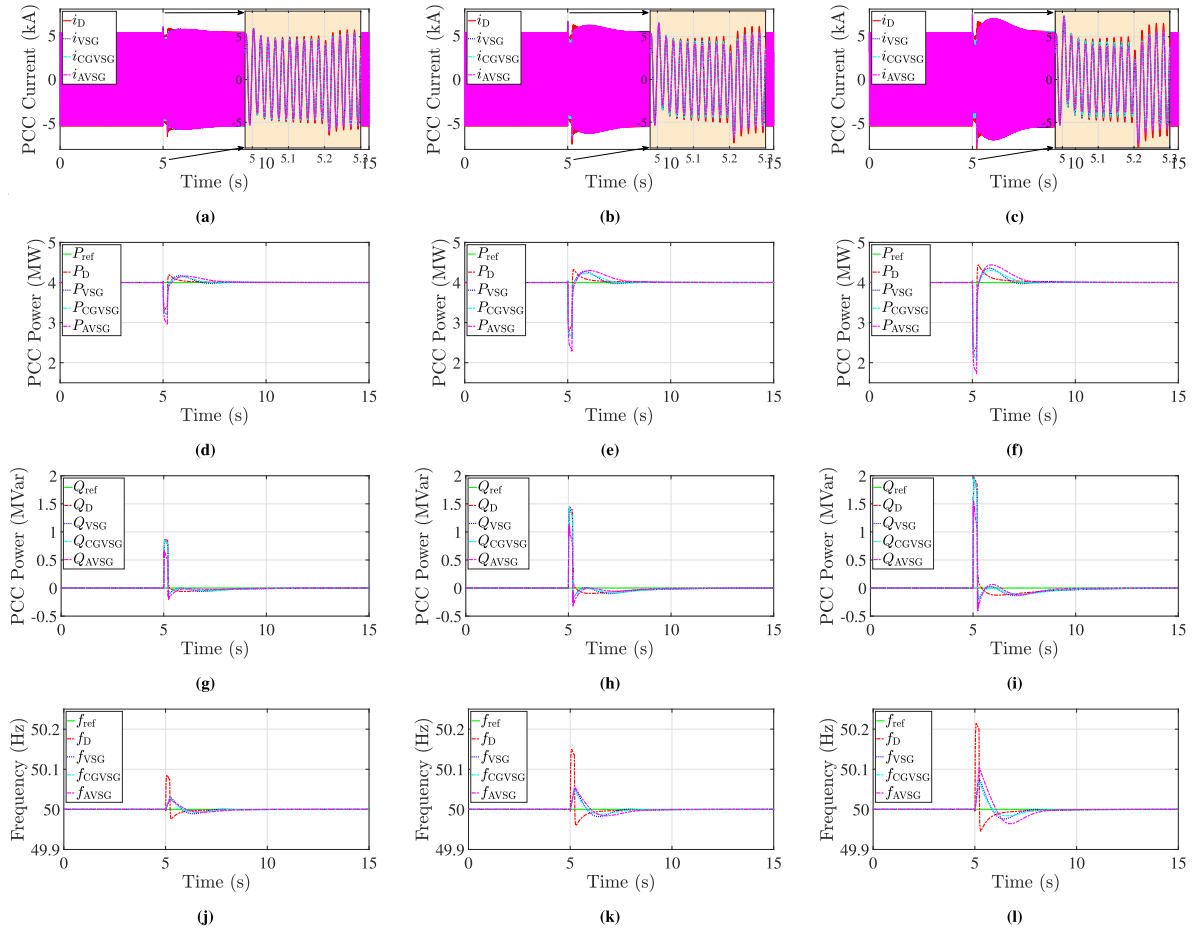


**FIGURE 15.** Performance of the GFMI in a weak grid ( $SCR = 1.5$ ,  $X_g/R_g = 7$ ) under symmetric voltage sag of the grid voltage source: (left)  $20\%V_g$ , (middle)  $35\%V_g$ , and (right)  $50\%V_g$ . (a)–(c) PCC current. (d)–(f) PCC active power. (g)–(i) PCC reactive power. (j)–(l) Frequency of the GFMI.

limitations, with exclusive emphasis placed on the primary loop response. The introduction of current limiters would result in extra dynamics being added to the inner control loops, leading to the limitation of over current, particularly for AVSG, as depicted in Fig. 16(a)–(c). Such behavior may be deemed unstable and is likely to be triggered by the current limiters. An analysis of the frequency plots in Fig. 16(l) reveals that the VSG reaches a peak just under 50.55 Hz, while the AVSG reaches almost 51 Hz. These frequency deviations may surpass the accepted tolerances in a power system, prompting the activation of frequency relays.

## 2) PHASE JUMP

Similar to the weak grid test, active and reactive power references are maintained at  $P_{ref} = 4$  MW and  $Q_{ref} = 0$  MVar throughout this assessment. Again, three distinct phase jumps are  $15^\circ$ ,  $30^\circ$ , and  $45^\circ$  and applied at 5 s to the three phases of the grid voltage source.

Throughout this evaluation, stable but distinct dynamic response patterns to these phase jumps are observed by the droop, VSG, CGVSG, and AVSG, as illustrated in Fig. 17. A few seconds after the occurrence of the 5-s phase jump,

these controllers settle back down to the reference commands. They have a much larger settling time when compared with the droop, which demonstrates very fast responses, effectively regulating active and reactive powers back to their steady-state values within less than 1 s after the phase jump disturbance.

Despite lower oscillations in active and reactive power responses exhibited by the AVSG, similar settling times are observed compared to the VSG and the CGVSG, as depicted in Fig. 11(f) and (i). Conversely, the VSG demonstrates highly oscillatory behavior with settling times exceeding 5 s in active power, reactive power, and frequency waveforms, as presented in Fig. 11. Notably, PCC currents experience undesirable transients, reaching heights of 15 kA, rendering VSG the most vulnerable controller to phase jumps in the grid voltage source, as shown in Fig. 17(c).

As illustrated in Fig. 11(j)–(l), the droop undergoes a rapid increase in frequency, surpassing 50.4 Hz and reaching 51.25 Hz with rapid RoCoF in response to phase jumps applied at 5 s. Despite effective control by the VSG and the CGVSG to limit frequency deviation, they exhibit relatively higher RoCoF values compared to the AVSG. Notably, the AVSG stands out for its exceptional robustness in managing

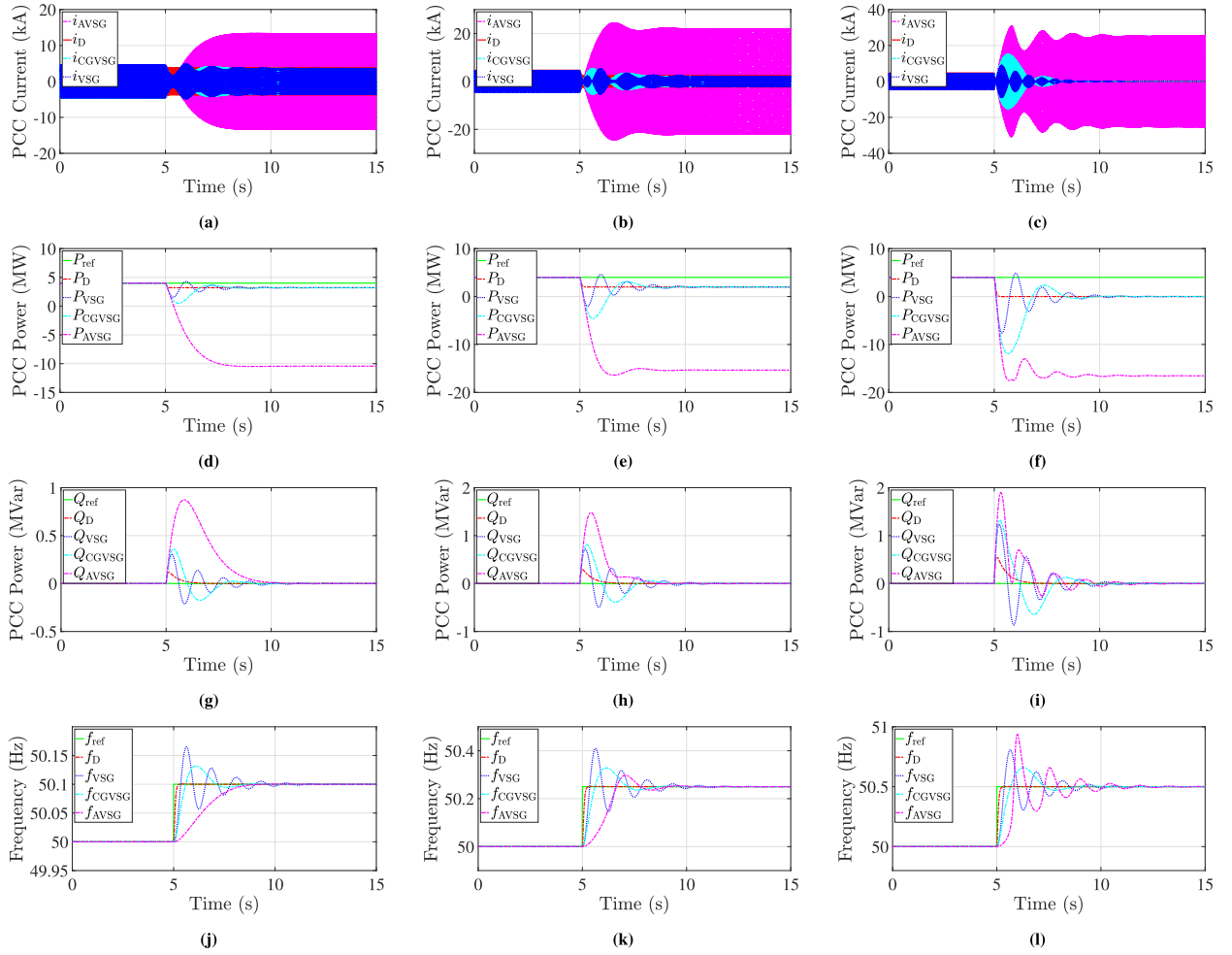


**FIGURE 16.** Performance of the GFMI in a strong grid ( $SCR = 8$ ,  $X_g/R_g = 7$ ) under frequency deviations of the grid voltage source: (left) 0.1 Hz, (middle) 0.25 Hz, and (right) 0.5 Hz. (a)–(c) PCC current. (d)–(f) PCC active power. (g)–(i) PCC reactive power. (j)–(l) Frequency of the GFMI.

frequency deviation, showcasing minimal overshoots and RoCoF.

### 3) VOLTAGE SAG

Fig. 18 illustrates the system responses during a symmetrical grid voltage sag, initiated at 5 s and lasting for 200 ms. Three distinct levels of voltage sags are explored in this test, with constant active and reactive power reference commands being maintained, consistent with the previous test. It is important to emphasize that these voltage sags are applied at a fixed  $X_g/R_g$  ratio of 7 throughout the entirety of the test.

With the exception of the VSG, robustness is exhibited by all the tested controllers even under the influence of a severe 50% voltage sag, as illustrated in Fig. 18(c), (f), (i), and (l), with acceptable settling times. In contrast, significant oscillations in active power tracking and frequency are manifested by the VSG, necessitating approximately 5 s for stabilization. Notably, these oscillations are less pronounced in the VSG's reactive power response. It is evident that, at 5 s, there is a sudden increase in reactive power injection to support the grid

during the voltage sag, in line with expectations. As the severity of the voltage sag increases, the amount of injected reactive power into the grid also rises. In the case of a 50% voltage sag, as depicted in Fig. 15(i), nearly 5 MVar of reactive power is injected by three VSG-based controllers, more than double the amount observed in the weak grid scenario.

In Fig. 15(j)–(l), abrupt changes in the frequency of the droop can be observed when the active power is reduced in response to the voltage sag. This high RoCoF behavior is similar to the previous frequency event-triggering cases considered in the time-domain study. However, much lower RoCoF values are portrayed by the CGVSG and the VSG compared to those of the droop. As observed in the previous case study of phase jumps, the AVSG displays robust performance against voltage sags with minimal frequency deviation.

## VI. SUMMARY AND RECOMMENDATIONS OF THE COMPARISON RESULTS

Table 3 presents a summary of the performance of the four control strategies for GFMI systems. This summary is derived from the results reported in the previous section for analysis in



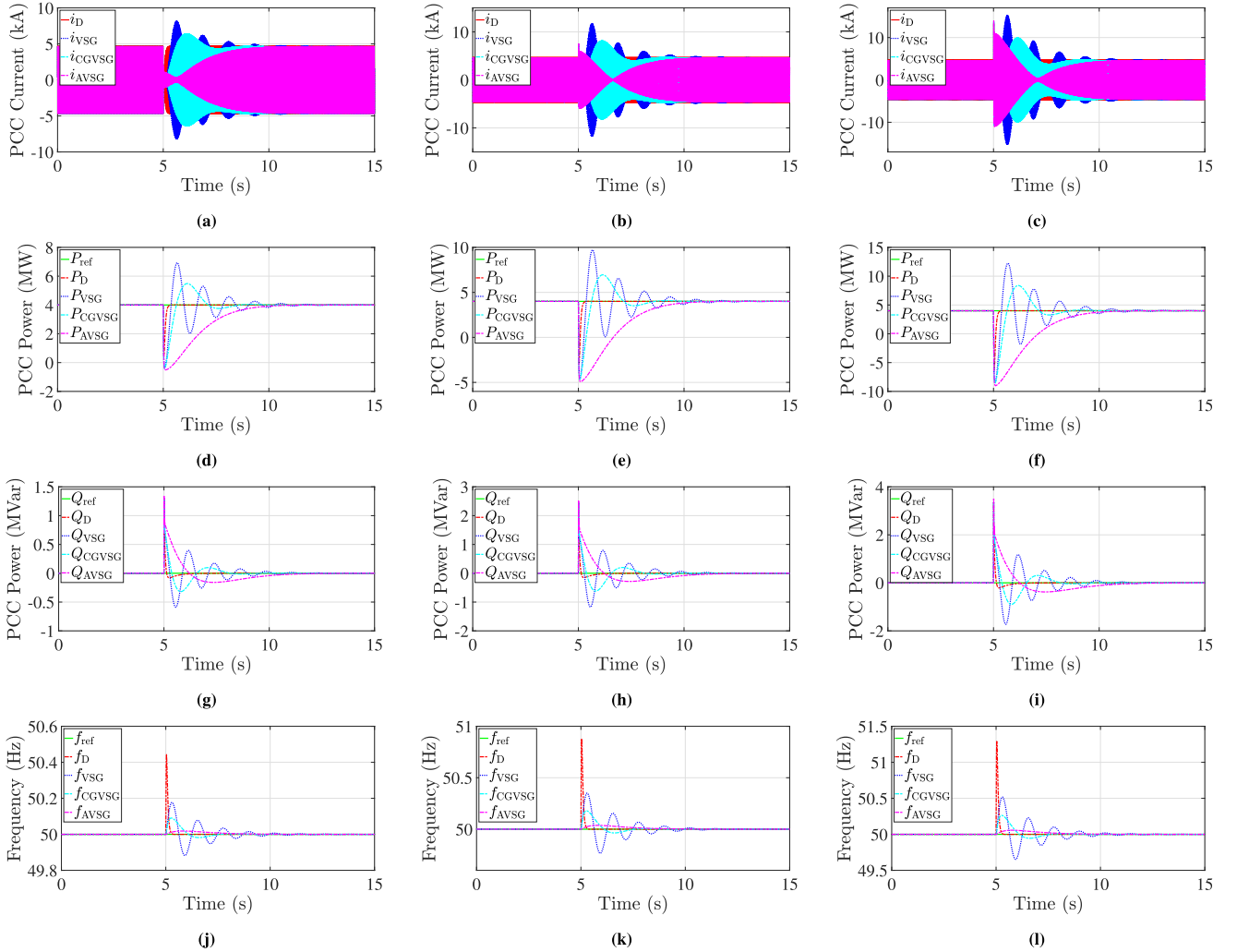


**FIGURE 17.** Performance of the GFMs in a strong grid ( $SCR = 8$ ,  $X_g/R_g = 7$ ) under phase jumps of the grid voltage source: (left)  $15^\circ$ , (middle)  $30^\circ$ , and (right)  $45^\circ$ . (a)–(c) PCC current. (d)–(f) PCC active power. (g)–(i) PCC reactive power. (j)–(l) Frequency of the GFMs.

both frequency and time domains considering different testing conditions. In general, superior performance in weak grid conditions is observed across all controllers, underscoring their GFM capability and support for weaker grids. Despite the droop controller demonstrating the fastest dynamic responses, the RoCoF limit tends to be violated due to the absence of inertia capability. Conversely, the VSG appears to be more oscillatory, particularly in strong grids with lower  $X_g/R_g$  ratios and under grid disturbances such as phase jumps and voltage sags. The CGVSG shows robust responses in most tested cases even under strong grid conditions. The AVSG also demonstrates promising responses in most of the considered test cases, characterized by good dynamic performance such as low overshoots and settling times, except for scenarios involving frequency deviations.

The following key observations are drawn for each considered test case.

- 1) *Active and reactive power control:* In the weak grid scenario, the accurate tracking of active and reactive power references with zero steady-state error is achieved by

all four controllers. Pronounced oscillations in power tracking are observed by all four controllers, especially by the VSG, at lower  $X_g/R_g$  ratios, resulting in longer settling times and higher power swing peaks. Conversely, undesired decoupling performance is demonstrated by the AVSG at the lowest  $X_g/R_g$  ratio, with considerable peaks in active power observed during reactive power reference changes. Frequency deviation during step response is characterized by sharp peaks in the droop due to the absence of inertia. In contrast, less RoCoF is displayed by the VSG-based controllers, with the AVSG outperforming others in frequency response. Transitioning to the strong grid scenario, active power references are effectively followed with minimal overshoots by the droop, followed by the CGVSG, with the AVSG showing over damped response. However, highly oscillatory behavior is exhibited by the VSG, particularly at lower  $X_g/R_g$  ratios. For frequency deviation during step response in power references, the AVSG stands out with the lowest overshoot and lowest RoCoF.

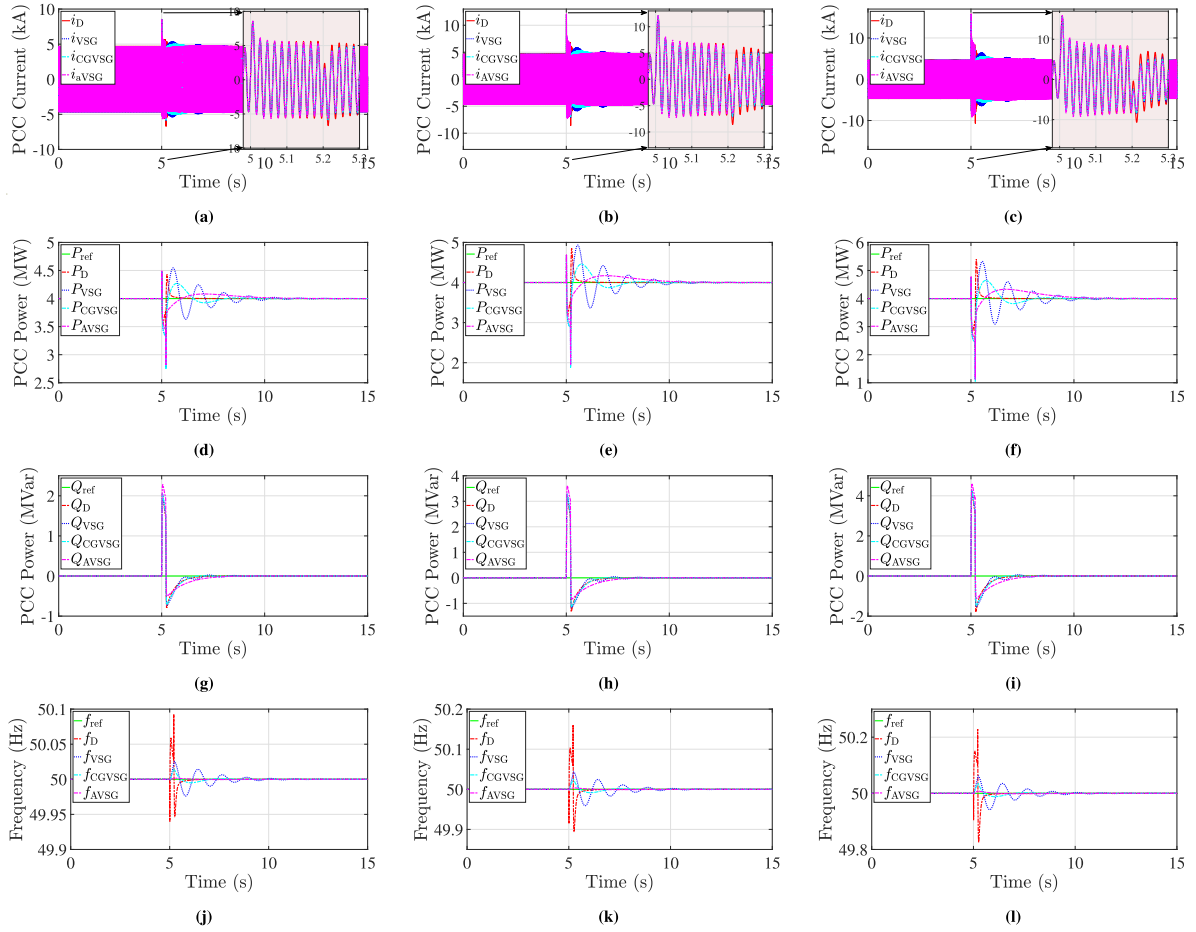


**FIGURE 18.** Performance of the GFMI in a strong grid ( $SCR = 8$ ,  $X_g/R_g = 7$ ) under symmetric voltage sag of the grid voltage source: (left)  $20\%V_g$ , (middle)  $35\%V_g$ , and (right)  $50\%V_g$ . (a)–(c) PCC current. (d)–(f) PCC active power. (g)–(i) PCC reactive power. (j)–(l) Frequency of the GFMI.

- 2) *Frequency deviations:* In the weak grid scenario, superior tracking of grid frequency changes with no overshoot is achieved by the droop method. Similar patterns of longer settling times and higher overshoots are exhibited by the VSG and the CGVSG. Subsequently, highly varied performance is demonstrated by the AVSG based on the severity of frequency deviations, with an oscillatory response for higher values of frequency deviations, showcasing its sensitivity to grid frequency disturbances due to adaptive tuning of the damping coefficient. Transitioning to the strong grid scenario, robust performance with no overshoot is once again demonstrated by the droop method, while large overshoots and longer settling times are observed for the VSG and the CGVSG. Finally, significant oscillations, especially associated with high frequency deviations, are exhibited by the AVSG, leading to much higher peaks and different steady-state values for output active and reactive power compared to other controllers.
- 3) *Phase jumps:* In the weak grid scenario, while no overshoots are exhibited in the inverter output current response to phase jumps by the droop, it displays high

RoCoF with severe frequency spikes, potentially exceeding safe transmission limits. Oscillatory behaviors are observed in both the VSG and the CGVSG, with nearly identical initial RoCoF values. Conversely, the AVSG outperforms other controllers in mitigating phase jump effects, displaying over damped waveforms and the lowest initial RoCoF. In the strong grid scenario, similar patterns emerge, with most controllers showing consistent initial power responses postphase jump. The droop demonstrates robust responses, returning to reference commands within 1 s. The VSG exhibits highly oscillatory behavior and extended settling times. The CGVSG exhibits minimal oscillation and slightly shorter settling times compared to the VSG, while the AVSG displays an overdamped response with a settling time resembling that of the VSG. Regarding frequency deviation during phase jump grid voltage (initial RoCoF), the droop experiences a rapid increase, while the VSG and the CGVSG show similar initial responses, with the VSG oscillating for a longer duration. Finally, the AVSG demonstrates superior robustness with minimal overshoots and RoCoF.

**TABLE 3. Comparison Summary of the Investigated Control Strategies of GFMI Operating in Different Conditions**

Criteria	Droop-based GFMI		VSG-based GFMI		CGVSG-based GFMI		AVSG-based GFMI	
	Weak Grid	Strong Grid	Weak Grid	Strong Grid	Weak Grid	Strong Grid	Weak Grid	Strong Grid
Step Response of Active Power	✓✓✓	✓✓✓	✓✓	✓	✓✓✓	✓✓✓	✓✓✓	✓✓✓
Step Response of Reactive Power	✓✓✓	✓✓✓	✓✓	✓	✓✓✓	✓✓✓	✓✓✓	✓✓
Frequency Deviation	✓✓✓	✓✓✓	✓✓	✓	✓✓	✓	✗	✗
Phase Jump	✓✓	✓✓	✓✓	✓	✓✓	✓✓	✓✓✓	✓✓✓
Grid Voltage Sag (Symmetric)	✓	✓	✓✓	✓	✓✓	✓✓	✓✓	✓✓✓
Inertia Support	✗	✗	✓✓	✓✓	✓✓✓	✓✓✓	✓✓✓	✓✓✓
Robustness Against $X_g/R_g$ ratio variations	✓✓✓	✓✓	✓	✗	✓✓✓	✓✓✓	✓✓✓	✓✓✓
Stability Margin Against Operating Point Variations	✓✓	✓✓	✓	✓	✓✓	✓✓	✓✓✓	✓✓✓

Levels of satisfaction of the controller performance: ✓✓✓ very well, ✓✓ good, ✓ accepted, ✗ poor (or unaccepted).

- 4) *Grid voltage sags*: In both weak and strong grid scenarios, robustness is demonstrated by all the tested controllers, even under severe voltage sag conditions. Significant oscillations are exhibited by the VSG and a longer settling time is required for stabilization, particularly in the strong grid scenario. During the voltage sag, a sudden increase in reactive power injection to support the grid is observed, and this increase becomes more significant as the severity of the voltage sag rises. The amount of reactive power injected in the strong grid case is considerably larger than that in a weak grid condition. Moreover, abrupt changes in the frequency of the droop occur when active power is reduced in response to the voltage sag, leading to a high RoCoF, which could trigger safety mechanisms. However, lower RoCoF values are exhibited by the CGVSG and the VSG compared to the droop. Robust performance against voltage sags is displayed by the AVSG, with the lowest RoCoF value observed in the strong grid scenario.
- 5) *Virtual impedance and inner loops*: The impacts of the virtual impedance and inner loops on power tracking are distinctly observed in weak and strong grids. In weak grid scenarios, similar and minimal impacts on the dynamic responses in active and reactive power tracking are observed by all controllers, particularly the droop and the CGVSG, irrespective of the presence or absence of the virtual impedance and inner loops. However, small couplings between active and reactive powers are observed without the virtual impedance. Conversely, in strong grids, controllers' power tracking responses are significantly influenced by the virtual impedance and inner loops, especially for the VSG, followed by the AVSG and the CGVSG, with relatively fewer impacts on droop. In addition, the presence of the virtual impedance suppresses oscillations during reactive power step changes when the inner loops are

present. In both weak and strong grid scenarios, similar features of all the controllers are exhibited in steady-state  $d$ -axis voltage values, influenced by the presence or absence of the virtual impedance and inner loops. The absence of both consistently results in the highest steady-state voltage.

The study uses frequency-domain analysis, along with time-domain analysis, to assess and validate small-signal stability of the control strategies under investigation. It includes a detailed examination in the  $dq$  reference frame for each control method, featuring Bode and Nyquist plots. The analysis covers both weak and strong grid conditions, exploring five operational scenarios. These scenarios involve variations in the grid's SCR, changes in the grid's impedance ratio, dynamics related to the virtual impedance, and the behavior of inner voltage and current loops. In addition, the study considers fluctuations in the inverter's active and reactive power references. This approach provides a thorough evaluation of small-signal stability, offering insights into the effectiveness of different control methods across diverse operational scenarios.

## VII. CONCLUSIONS

GFMI, as a promising solution, are being introduced into modern power systems, offering enhanced operational stability compared to GFLI, particularly in scenarios involving weak grids. GFMI have the capacity to provide crucial inertia and frequency support to the grid, especially during disturbance events. Four distinct control methodologies employed in the primary loop of GFMI, namely, droop-based GFMI, VSG-based GFMI, CGVSG-based GFMI, and AVSG-based GFMI, are comprehensively investigated in this article. The investigation is conducted in the frequency domain, utilizing both Bode and Nyquist plots in the  $dq$  reference frame, as well as in the time domain, aiming to provide valuable insights into the behavior of the four control techniques, shedding

light on their strengths and weaknesses in various operational scenarios.

Various operational scenarios are considered in this investigation, accounting for variations in the grid SCR, grid impedance ratio, dynamics related to the virtual impedance and inner voltage and current loop behavior, as well as step changes in inverter's active and reactive power references. Time-domain simulations based on electromagnetic transient models in MATLAB/Simulink are performed to validate the findings derived from the frequency-domain analysis. Furthermore, rigorous evaluations of external grid disturbances, such as grid frequency deviations, grid phase jumps, and grid voltage sags, are conducted through time-domain simulations to comprehensively assess the aforementioned control strategies in scenarios involving both weak and strong grid connections. The insights presented in this article serve as valuable guidance for the selection of the most suitable control methodology for GFMI in practical applications.

## REFERENCES

- [1] J. Matevosyan et al., "A future with inverter-based resources: Finding strength from traditional weakness," *IEEE Power Energy Mag.*, vol. 19, no. 6, pp. 18–28, Nov./Dec. 2021.
- [2] M. S. Mastoi, S. Zhuang, M. Haris, M. Hassan, and A. Ali, "Large-scale wind power grid integration challenges and their solution: A detailed review," *Environ. Sci. Pollut. Res.*, vol. 30, no. 47, pp. 103424–103462, Oct. 2023.
- [3] J. Z. Zhou, H. Ding, S. Fan, Y. Zhang, and A. M. Gole, "Impact of short-circuit ratio and phase-locked-loop parameters on the small-signal behavior of a VSC-HVDC converter," *IEEE Trans. Power Del.*, vol. 29, no. 5, pp. 2287–2296, Oct. 2014.
- [4] Y. Li, Y. Gu, and T. C. Green, "Revisiting grid-forming and grid-following inverters: A duality theory," *IEEE Trans. Power Syst.*, vol. 37, no. 6, pp. 4541–4554, Nov. 2022.
- [5] D. B. Rathnayake et al., "Grid forming inverter modeling, control, and applications," *IEEE Access*, vol. 9, pp. 114781–114807, 2021.
- [6] D. Sharma, F. Sadeque, and B. Mirafzal, "Synchronization of inverters in grid forming mode," *IEEE Access*, vol. 10, pp. 41341–41351, 2022.
- [7] S. Anttila, J. S. Döhler, J. G. Oliveira, and C. Boström, "Grid forming inverters: A review of the state of the art of key elements for microgrid operation," *Energies*, vol. 15, no. 15, 2022, Art. no. 5517.
- [8] R. H. Lasseter, Z. Chen, and D. Pattabiraman, "Grid-forming inverters: A critical asset for the power grid," *IEEE Trans. Emerg. Sel. Topics Power Electron.*, vol. 8, no. 2, pp. 925–935, Jun. 2020.
- [9] R. Rosso, X. Wang, M. Liserre, X. Lu, and S. Engelken, "Grid-forming converters: An overview of control approaches and future trends," in *Proc. IEEE Energy Convers. Congr. Expo.*, 2020, pp. 4292–4299.
- [10] K. De Brabandere, B. Bolsens, J. Van den Keybus, A. Woyte, J. Driesen, and R. Belmans, "A voltage and frequency droop control method for parallel inverters," *IEEE Trans. Power Electron.*, vol. 22, no. 4, pp. 1107–1115, Jul. 2007.
- [11] T. Vandoorn, J. De Koning, B. Meersman, and L. Vandevelde, "Review of primary control strategies for islanded microgrids with power-electronic interfaces," *Renewable Sustain. Energy Rev.*, vol. 19, pp. 613–628, 2013.
- [12] R. Majumder, B. Chaudhuri, A. Ghosh, R. Majumder, G. Ledwich, and F. Zare, "Improvement of stability and load sharing in an autonomous microgrid using supplementary droop control loop," *IEEE Trans. Power Syst.*, vol. 25, no. 2, pp. 796–808, May 2010.
- [13] J. Hu, J. Zhu, D. G. Dorrell, and J. M. Guerrero, "Virtual flux droop method—A new control strategy of inverters in microgrids," *IEEE Trans. Power Electron.*, vol. 29, no. 9, pp. 4704–4711, Sep. 2014.
- [14] L. Zhang, L. Harnefors, and H.-P. Nee, "Power-synchronization control of grid-connected voltage-source converters," *IEEE Trans. Power Syst.*, vol. 25, no. 2, pp. 809–820, May 2010.
- [15] L. Harnefors, M. Hinkkanen, U. Riaz, F. M. Rahman, and L. Zhang, "Robust analytic design of power-synchronization control," *IEEE Trans. Ind. Electron.*, vol. 66, no. 8, pp. 5810–5819, Aug. 2019.
- [16] H.-P. Beck and R. Hesse, "Virtual synchronous machine," in *Proc. 9th Int. Conf. Elect. Power Qual. Utilisation*, 2007, pp. 1–6.
- [17] Y. Chen, R. Hesse, D. Turschner, and H.-P. Beck, "Comparison of methods for implementing virtual synchronous machine on inverters," in *Proc. Int. Conf. Renewable Energies Power Qual.*, vol. 1, no. 10, pp. 734–739, 2012.
- [18] J. Driesen and K. Visscher, "Virtual synchronous generators," in *Proc. IEEE Power Energy Soc. Gen. Meeting—Convers. Del. Elect. Energy 21st Century*, 2008, pp. 1–3.
- [19] M. Guan, W. Pan, J. Zhang, Q. Hao, J. Cheng, and X. Zheng, "Synchronous generator emulation control strategy for voltage source converter (VSC) stations," *IEEE Trans. Power Syst.*, vol. 30, no. 6, pp. 3093–3101, Nov. 2015.
- [20] Q.-C. Zhong and G. Weiss, "Synchroverters: Inverters that mimic synchronous generators," *IEEE Trans. Ind. Electron.*, vol. 58, no. 4, pp. 1259–1267, Apr. 2011.
- [21] X. Wang, L. Chen, D. Sun, L. Zhang, and H. Nian, "A modified self-synchronized synchroverter in unbalanced power grids with balanced currents and restrained power ripples," *Energies*, vol. 12, no. 5, 2019, Art. no. 923.
- [22] B. B. Johnson, S. V. Dhople, A. O. Hamadeh, and P. T. Krein, "Synchronization of parallel single-phase inverters with virtual oscillator control," *IEEE Trans. Power Electron.*, vol. 29, no. 11, pp. 6124–6138, Nov. 2014.
- [23] B. B. Johnson, M. Sinha, N. G. Ainsworth, F. Dörfler, and S. V. Dhople, "Synthesizing virtual oscillators to control islanded inverters," *IEEE Trans. Power Electron.*, vol. 31, no. 8, pp. 6002–6015, Aug. 2016.
- [24] D. B. Rathnayake and B. Bahrani, "Multivariable control design for grid-forming inverters with decoupled active and reactive power loops," *IEEE Trans. Power Electron.*, vol. 38, no. 2, pp. 1635–1649, Feb. 2023.
- [25] S. S. Madani, C. Kammer, and A. Karimi, "Data-driven distributed combined primary and secondary control in microgrids," *IEEE Trans. Control Syst. Technol.*, vol. 29, no. 3, pp. 1340–1347, May 2021.
- [26] L. Huang et al., "A virtual synchronous control for voltage-source converters utilizing dynamics of DC-link capacitor to realize self-synchronization," *IEEE Trans. Emerg. Sel. Topics Power Electron.*, vol. 5, no. 4, pp. 1565–1577, Dec. 2017.
- [27] B. Shakerighadi et al., "An overview of stability challenges for power-electronic-dominated power systems: The grid-forming approach," *IET Gener., Transmiss. Distrib.*, vol. 17, no. 2, pp. 284–306, 2023.
- [28] D. B. Rathnayake, R. Razzaghi, and B. Bahrani, "Generalized virtual synchronous generator control design for renewable power systems," *IEEE Trans. Sustain. Energy*, vol. 13, no. 2, pp. 1021–1036, Apr. 2022.
- [29] N. Mohammed, M. H. Ravanji, W. Zhou, and B. Bahrani, "Online grid impedance estimation-based adaptive control of virtual synchronous generators considering strong and weak grid conditions," *IEEE Trans. Sustain. Energy*, vol. 14, no. 1, pp. 673–687, Jan. 2023.
- [30] N. Mohammed, W. Zhou, and B. Bahrani, "Comparison of PLL-based and PLL-less control strategies for grid-following inverters considering time and frequency domain analysis," *IEEE Access*, vol. 10, pp. 80518–80538, 2022.
- [31] S. M. Hoseinizadeh, S. Ouni, H. Karimi, M. Karimi-Ghartemani, and K. L. Lian, "Comparison of PLL-based and PLL-less vector current controllers," *IEEE Trans. Emerg. Sel. Topics Power Electron.*, vol. 10, no. 1, pp. 436–445, Feb. 2022.
- [32] R. Rosso, X. Wang, M. Liserre, X. Lu, and S. Engelken, "Grid-forming converters: Control approaches, grid-synchronization, and future trends—A review," *IEEE Open J. Ind. Appl.*, vol. 2, pp. 93–109, 2021.
- [33] P. Unruh, M. Nuschke, P. Strauß, and F. Welck, "Overview on grid-forming inverter control methods," *Energies*, vol. 13, no. 10, 2020, Art. no. 2589.
- [34] E. Bikkdeli, M. R. Islam, M. M. Rahman, and K. M. Muttaqi, "State of the art of the techniques for grid forming inverters to solve the challenges of renewable rich power grids," *Energies*, vol. 15, no. 5, 2022, Art. no. 1879.
- [35] G. Song, B. Cao, and L. Chang, "Review of grid-forming inverters in support of power system operation," *Chin. J. Elect. Eng.*, vol. 8, no. 1, pp. 1–15, 2022.



- [36] M. Awal, H. Yu, S. Lukic, and I. Husain, "Droop and oscillator based grid-forming converter controls: A comparative performance analysis," *Front. Energy Res.*, vol. 8, 2020, Art. no. 168.
- [37] A. Alassi, K. Ahmed, A. Egea-Alvarez, and O. Ellabban, "Performance evaluation of four grid-forming control techniques with soft black-start capabilities," in *Proc. 9th Int. Conf. Renewable Energy Res. Appl.*, 2020, pp. 221–226.
- [38] J. Liu, Y. Miura, and T. Ise, "Comparison of dynamic characteristics between virtual synchronous generator and droop control in inverter-based distributed generators," *IEEE Trans. Power Electron.*, vol. 31, no. 5, pp. 3600–3611, May 2016.
- [39] D. Aragon, E. Unamuno, S. Ceballos, and J. Barrena, "Comparative small-signal evaluation of advanced grid-forming control techniques," *Electr. Power Syst. Res.*, vol. 211, 2022, Art. no. 108154.
- [40] Y. Qi, H. Deng, J. Fang, and Y. Tang, "Synchronization stability analysis of grid-forming inverter: A black box methodology," *IEEE Trans. Ind. Electron.*, vol. 69, no. 12, pp. 13069–13078, Dec. 2022.
- [41] W. Du et al., "A comparative study of two widely used grid-forming droop controls on microgrid small-signal stability," *IEEE Trans. Emerg. Sel. Topics Power Electron.*, vol. 8, no. 2, pp. 963–975, Jun. 2020.
- [42] Y. Gu and T. C. Green, "Power system stability with a high penetration of inverter-based resources," in *Proc. IEEE*, vol. 111, no. 7, pp. 832–853, Jul. 2022.
- [43] D. Pan, X. Wang, F. Liu, and R. Shi, "Transient stability of voltage-source converters with grid-forming control: A design-oriented study," *IEEE Trans. Emerg. Sel. Topics Power Electron.*, vol. 8, no. 2, pp. 1019–1033, Jun. 2020.
- [44] T. Qoria, F. Gruson, F. Colas, X. Kestelyn, and X. Guillaud, "Current limiting algorithms and transient stability analysis of grid-forming VSCs," *Electr. Power Syst. Res.*, vol. 189, 2020, Art. no. 106726.
- [45] M. H. Ravanji, D. B. Rathnayake, M. Z. Mansour, and B. Bahrani, "Impact of voltage-loop feedforward terms on the stability of grid-forming inverters and remedial actions," *IEEE Trans. Energy Convers.*, vol. 38, no. 3, pp. 1554–1565, Sep. 2023.
- [46] J. M. Guerrero, L. G. De Vicuna, J. Matas, M. Castilla, and J. Miret, "Output impedance design of parallel-connected UPS inverters with wireless load-sharing control," *IEEE Trans. Ind. Electron.*, vol. 52, no. 4, pp. 1126–1135, Aug. 2005.
- [47] J. M. Guerrero, J. C. Vasquez, J. Matas, L. G. De Vicuña, and M. Castilla, "Hierarchical control of droop-controlled ac and dc microgrids—A general approach toward standardization," *IEEE Trans. Ind. Electron.*, vol. 58, no. 1, pp. 158–172, Jan. 2011.
- [48] X. Wang, Y. W. Li, F. Blaabjerg, and P. C. Loh, "Virtual-impedance-based control for voltage-source and current-source converters," *IEEE Trans. Power Electron.*, vol. 30, no. 12, pp. 7019–7037, Dec. 2015.
- [49] N. Mohammed, A. Lashab, M. Ciobotaru, and J. M. Guerrero, "Accurate reactive power sharing strategy for droop-based islanded ac microgrids," *IEEE Trans. Ind. Electron.*, vol. 70, no. 3, pp. 2696–2707, Mar. 2023.
- [50] J. M. Guerrero, J. Matas, L. G. de Vicuna, M. Castilla, and J. Miret, "Decentralized control for parallel operation of distributed generation inverters using resistive output impedance," *IEEE Trans. Ind. Electron.*, vol. 54, no. 2, pp. 994–1004, Apr. 2007.
- [51] J. M. Alcalá, M. Castilla, L. G. De Vicuña, J. Miret, and J. C. Vasquez, "Virtual impedance loop for droop-controlled single-phase parallel inverters using a second-order general-integrator scheme," *IEEE Trans. Power Electron.*, vol. 25, no. 12, pp. 2993–3002, Dec. 2010.
- [52] J. He and Y. W. Li, "Analysis, design, and implementation of virtual impedance for power electronics interfaced distributed generation," *IEEE Trans. Ind. Appl.*, vol. 47, no. 6, pp. 2525–2538, Nov./Dec. 2011.
- [53] J. He, Y. W. Li, J. M. Guerrero, F. Blaabjerg, and J. C. Vasquez, "An islanding microgrid power sharing approach using enhanced virtual impedance control scheme," *IEEE Trans. Power Electron.*, vol. 28, no. 11, pp. 5272–5282, Nov. 2013.
- [54] H. Mahmood, D. Michaelson, and J. Jiang, "Accurate reactive power sharing in an islanded microgrid using adaptive virtual impedances," *IEEE Trans. Power Electron.*, vol. 30, no. 3, pp. 1605–1617, Mar. 2015.
- [55] M. C. Chandorkar, D. M. Divan, and R. Adapa, "Control of parallel connected inverters in standalone ac supply systems," *IEEE Trans. Ind. Appl.*, vol. 29, no. 1, pp. 136–143, Jan./Feb. 1993.
- [56] M. Nichol, "System Rate of Change of Frequency—A GHD survey of international views," GHD Pty Ltd., Melbourne, VIC, Australia, Tech. Rep. 12587342, 2022.
- [57] N. Al-Masood, N. Modi, and R. Yan, "Low inertia power systems: Frequency response challenges and a possible solution," in *Proc. IEEE Australas. Univ. Power Eng. Conf.*, 2016, pp. 1–6.
- [58] J. Sun, "Impedance-based stability criterion for grid-connected inverters," *IEEE Trans. Power Electron.*, vol. 26, no. 11, pp. 3075–3078, Nov. 2011.
- [59] I. Ray, "Review of impedance-based analysis methods applied to grid-forming inverters in inverter-dominated grids," *Energies*, vol. 14, no. 9, 2021, Art. no. 2686.
- [60] K. Oue, S. Sano, T. Kato, and K. Inoue, "Stability analysis of grid-forming inverter in DQ frequency domain," in *Proc. 20th Workshop Control Model. Power Electron.*, 2019, pp. 1–8.
- [61] W. Cao, Y. Ma, L. Yang, F. Wang, and L. M. Tolbert, "D-Q impedance based stability analysis and parameter design of three-phase inverter-based ac power systems," *IEEE Trans. Ind. Electron.*, vol. 64, no. 7, pp. 6017–6028, Jul. 2017.
- [62] B. Wen, R. Burgos, D. Boroyevich, P. Mattavelli, and Z. Shen, "AC stability analysis and DQ frame impedance specifications in power-electronics-based distributed power systems," *IEEE Trans. Emerg. Sel. Topics Power Electron.*, vol. 5, no. 4, pp. 1455–1465, Dec. 2017.
- [63] R. Luhtala, T. Roinila, and T. Messo, "Implementation of real-time impedance-based stability assessment of grid-connected systems using MIMO-identification techniques," *IEEE Trans. Ind. Appl.*, vol. 54, no. 5, pp. 5054–5063, Sep./Oct. 2018.
- [64] Y. Liao and X. Wang, "General rules of using bode plots for impedance-based stability analysis," in *Proc. IEEE 19th Workshop Control Model. Power Electron.*, 2018, pp. 1–6.
- [65] Y. Liao and X. Wang, "General rules of using bode plots for impedance-based stability analysis," in *Proc. IEEE 19th Workshop Control Model. Power Electron.*, 2018, pp. 1–6.
- [66] Y. Liao and X. Wang, "Impedance-based stability analysis for interconnected converter systems with open-loop RHP poles," *IEEE Trans. Power Electron.*, vol. 35, no. 4, pp. 4388–4397, Apr. 2020.
- [67] A. A. A. Radwan and Y. A.-R.I. Mohamed, "Improved vector control strategy for current-source converters connected to very weak grids," *IEEE Trans. Power Syst.*, vol. 31, no. 4, pp. 3238–3248, Jul. 2016.
- [68] Y. Wang, M. H. Bollen, and X.-Y. Xiao, "Calculation of the phase-angle-jump for voltage dips in three-phase systems," *IEEE Trans. Power Del.*, vol. 30, no. 1, pp. 480–487, Feb. 2015.



**NABIL MOHAMMED** (Senior Member, IEEE) received the bachelor's (Hons.) degree in electrical power engineering from Tishreen University, Latakia, Syria, in 2013, the M.Eng. degree in electrical engineering from Universiti Teknologi Malaysia, Johor Bahru, Malaysia, in 2017, and the Ph.D. degree in power electronics from Macquarie University, Sydney, NSW, Australia, in 2022.

During the summer of 2019, he was a Visiting Researcher with the Department of Energy Technology, Aalborg University, Aalborg, Denmark. He is currently a Postdoctoral Research Fellow with Monash University, Clayton, VIC, Australia. His research interests include power electronics, grid integration of renewable energy resources, microgrids, energy storage and management systems, and modeling and control of electric power systems.



**HARITH UDAWATTE** (Graduate Student Member, IEEE) received the B.Sc. degree in electrical and electronic engineering from the University of Peradeniya, Peradeniya, Sri Lanka, in 2021. He is currently working toward the Ph.D. degree in electrical engineering with Monash University, Clayton, VIC, Australia.

During his Ph.D. studies, he is also actively involved in research on developing Australia's Global Power System Transformation Research Roadmap, published by CSIRO in collaboration with the Global Power System Transformation Consortium. His research interests include the control and stability analysis of grid-following and grid-forming inverter-based resources, as well as the grid integration of renewable energy sources, with a particular emphasis on wind energy.



**WEIHUA ZHOU** (Member, IEEE) received the B.Eng. degree in electrical engineering from the Honors College, Northwestern Polytechnical University, Xi'an, China, in 2014, the M.Sc. degree in electrical engineering from the School of Automation, Northwestern Polytechnical University, in 2017, and the Ph.D. degree in power electronics from the Department of Energy Technology, Aalborg University, Aalborg, Denmark, in 2020.

From 2015 to 2016, he was a Junior Research Assistant with the Department of Mechanical and Automation Engineering, The Chinese University of Hong Kong, Hong Kong. From August 2020 to November 2020, he was a Visiting Scholar with the Department of Marine Technology, Norwegian University of Science and Technology, Trondheim, Norway. In 2021, he was a Research Fellow with the Department of Electrical Engineering, Katholieke Universiteit Leuven, Leuven, Belgium. He is currently a Research Fellow with the Department of Electrical and Computer Systems Engineering, Monash University, Clayton, VIC, Australia. His research interests include modeling, analysis, and control of power-electronic-based modern power systems.



**DAVID J. HILL** (Life Fellow, IEEE) received the Ph.D. degree in electrical engineering from the University of Newcastle, Callaghan, NSW, Australia, in 1976.

Since 2022, he has been a Professor of Electrical Power and Energy Systems with Monash University, Clayton, VIC, Australia. He is also Professor Emeritus with the University of Sydney, Camperdown, NSW, and the University of Hong Kong, Hong Kong. From 2013 to 2020, he was a Chair of Electrical Engineering and the Director of the Centre for Electrical Energy Systems with the Department of Electrical and Electronic Engineering, The University of Hong Kong. He previously held positions with the University of Sydney, including the Chair of Electrical Engineering from 1994 to 2002 and from 2010 to 2013 along with an Australian Research Council Professorial Fellowship. He was a Foundation Director of the Centre for Future Energy Networks from 2010 to 2018 and a Part-Time Professor from 2013 to 2020. From 2005 to 2010, he was an ARC Federation Fellow with the Australian National University, Canberra, ACT, Australia. He has also held academic and substantial visiting positions with the University of Melbourne, Melbourne, VIC; the University of California, Berkeley, CA, USA; the University of Newcastle; Lund University, Lund, Sweden; the University of Munich, Munich, Germany; the City University of Hong Kong, Hong Kong; and the University of New South Wales, Sydney, NSW. He has held several honorary positions in Australia, Hong Kong, and Mainland China. He is also a consultant in the area of power and energy issues in Australia and internationally. His work is now mainly focused on issues for future energy and power networks with the aim to bring science to accelerate the clean energy transition. His research interests include energy and power systems, control systems, complex networks and systems, learning systems, and stability analysis.

Dr. Hill was the recipient of the 2021 IEEE Power and Energy Society Prabha S. Kundur Power System Dynamics and Control Award and the 2022 IEEE Control System Society Hendrik W. Bode Lecture Prize. He is a Fellow of the Society for Industrial and Applied Mathematics, the International Federation of Automatic Control, the Australian Academy of Science, the Australian Academy of Technological Sciences and Engineering, and the Hong Kong Academy of Engineering Sciences. He is also a Foreign Member of the Royal Swedish Academy of Engineering Sciences.



**BEHROOZ BAHRANI** (Senior Member, IEEE) received the B.Sc. degree from the Sharif University of Technology, Tehran, Iran, in 2006, the M.Sc. degree from the University of Toronto, Toronto, ON, Canada, in 2008, and the Ph.D. degree from the Ecole Polytechnique Fédérale de Lausanne, Lausanne, Switzerland, in 2012, all in electrical engineering.

From 2012 to 2015, he was a Postdoctoral Fellow with several institutions, including the Swiss Federal Institute of Technology Lausanne, Lausanne, Switzerland; Purdue University, West Lafayette, IN, USA; Georgia Institute of Technology, Atlanta, GA, USA; and the Technical University of Munich, Munich, Germany. Since 2015, he has been with Monash University, Clayton, VIC, Australia, where he is currently an Associate Professor and the Director of the Grid Innovation Hub. His research interests include control of power electronic systems, applications of power electronics in power and traction systems, and grid integration of renewable energy resources.